Document Version
Final published version

Licence
CC BY

Citation (APA)
Tu, W., Pascoe, J. A., & Alderliesten, R. (2026). Comparison between 1D and 2D delamination growth in composite laminates: An experimental and numerical investigation. *Composites Part B: Engineering*, *324*, Article 113836. https://doi.org/10.1016/j.compositesb.2026.113836

Composites Part B 324 (2026) 113836

Contents lists available at ScienceDirect

Composites Part B

journal homepage: www.elsevier.com/locate/composites

Comparison between 1D and 2D delamination growth in composite laminates: An experimental and numerical investigation

Wenjie Tu *, John-Alan Pascoe, René Alderliesten

Department of Aerospace Structures and Materials, Faculty of Aerospace Engineering, Delft University of Technology, Kluyverweg 1, Delft, 2629HS, The Netherlands

ARTICLE INFO

Dataset link: https://doi.org/10.4121/ec008223-1408-481db641-d6e7903dd594

Keywords:
Delamination
Polymer-matrix composites (PMC)
Finite element analysis (FEA)
Fibre bridging
Fractography

ABSTRACT

Delamination growth in composite laminates is essentially two-dimensional (2D), indicating a multidirectional spreading of interlaminar damage. However, the evaluation and prediction of delamination growth mainly relies on the quantification of one-dimensional (1D) growth using unidirectional specimens. In this study, the discrepancies and similarities between 1D and 2D delamination behaviours of composite laminates are investigated, both experimentally and numerically. The fracture toughness of mode II delamination, measured experimentally through 1D tests, is compared with the numerically fitted critical Energy Release Rate (ERR) in 2D delamination using Cohesive Zone Modelling (CZM) method. The fracture mechanisms involved in 1D and 2D delamination growth are investigated through fractography at the delamination interfaces. Although similar damage mechanisms are present in 1D and 2D tests, using the fracture toughness measured from 1D tests to predict 2D growth is proven to be insufficient due to distinct extrinsic toughening effects. Variations in local stress states significantly influence delamination growth, necessitating different cohesive constitutive models to accurately describe 1D and 2D delamination processes.

1. Introduction

In order to assess the structural hazard posed by delamination, its severity must be evaluated. In Carbon Fibre-reinforced Polymer (CFRP) composites particularly, delamination occurs at the laminate interface and is not visible to the naked eye. Non-destructive inspection methods, such as ultrasound scanning (primarily C-scan mapping [1,2]) and X-ray computed tomography (CT-scan) [3,4], are commonly employed to study the morphology of multiple delaminations. A typical impact damage scenario visualised by a μ-CT scan is shown in Fig. 1. Multiple delaminations are located at various interfaces and depths. Delamination growth generally follows the fibre orientation of the adjacent ply, resulting in a petal-shaped delamination pattern. The overlapping of delaminations complicates the determination of the actual damage area within the damage envelope [5]. Delamination growth in such damage scenarios is inherently multidirectional and must be addressed as a two-dimensional (2D) problem. In contrast, standardised coupon tests simplify delamination to a one-dimensional (1D) phenomenon, characterising size solely by delamination or crack length, such as Double Cantilever Beam (DCB [6]) and End-notched Split (ENF [7]) tests.

Given the presence of multiple delamination interfaces in impact-induced damage, the influence of interface angles on fracture resistance has garnered increasing attention. Depending on the loading conditions, variations in interface angles have been shown to affect both delamination behaviour and fracture resistance [8–10]. A tortuous delamination path (under mode I loading [11]) or delamination migration (under mode II loading [12]) may occur when the delamination growth direction does not align with the ply orientation. This behaviour enhances fracture resistance (R-curve behaviour) due to significant intralaminar matrix cracking, development of a Fracture Process Zone (FPZ) and fibre bridging. Based on 1D delamination tests, the use of MD laminates with tailored stacking sequences offers the potential for improved structural design to enhance damage tolerance [10,13]. However, this approach is effective only if specific fracture modes are activated under service condition and the fracture mechanisms observed in actual damage scenarios are reproducible.

Previous studies have shown that extrinsic fracture toughness, primarily governed by fibre bridging and interfacial friction, is significantly influenced by interface angles, specimen configurations, and test conditions [14–18]. Consequently, using fracture toughness derived from standardised experiments with unidirectional (UD) specimens may result in inaccurate predictions of delamination growth at angled interfaces, where distinct toughening mechanisms arise from variations in local stress states [19,20]. Despite these variations, numerical predictions of delamination growth continue to rely on fracture toughness

---

* Corresponding author.
E-mail address: J.A.Pascoe@tudelft.nl (W. Tu).

https://doi.org/10.1016/j.compositesb.2026.113836
Received 30 September 2025; Received in revised form 8 December 2025; Accepted 19 May 2026

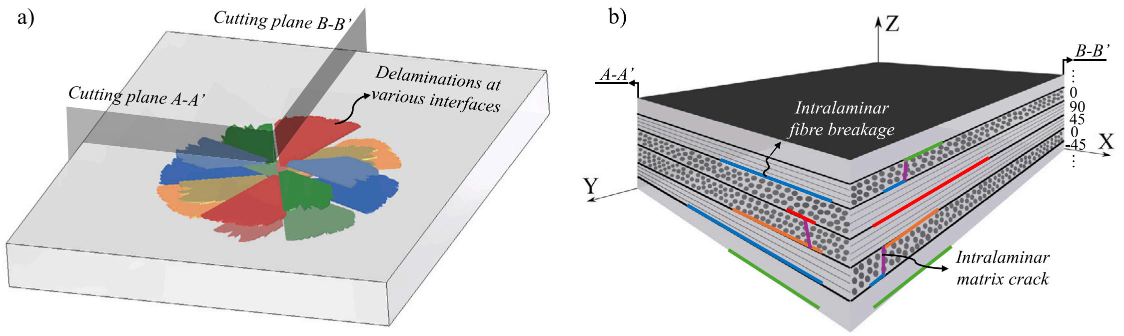

Fig. 1. (a) Typical impact induced delamination pattern extracted from CT-scan (adapted from [3]). (b) Cross-sectional view of the damage.

values obtained from standard 1D tests using UD laminates [21–25]. Although these simulations effectively capture the overall delamination behaviours, including patterns and propagation trends, a quantitative gap remains between the predicted results and the actual delamination growth.

Significant research efforts have been devoted to developing numerical tools to accurately capture delamination behaviour and the interactions between intralaminar and interlaminar damage modes [26–31]. Only few studies explicitly assess the applicability of fracture toughness values obtained from standard tests when simulating delamination growth in non-standard specimen configurations [18,32,33]. Wang et al. [18] developed a modified cohesive model to investigate differences in cohesive constitutive behaviour between 1D and 2D delamination in glass-fibre composite laminates. In that study, a constant total fracture toughness measured from 1D coupon tests was applied to simulate both 1D and 2D delamination growth. The fracture toughness at the tip of the delamination front was treated as a constant, while the remaining contributions to the energy release rate (ERR), including those associated with the evolution of the FPZ and fibre bridging, differed between 1D and 2D delamination behaviours. However, the determination of the different ERR components remains empirical and relies on experimental data for calibration.

In practical applications, it is challenging to ensure that a fully developed FPZ and fibre bridging zone exist in composite structures when delamination occurs. As a result, fracture toughness values determined using standard testing methods, which includes contributions from FPZ and fibre bridging, may not be directly applied to assess 2D delamination growth, as these contributions differ between configurations. The extent to which such fracture toughness values can be reliably used for predicting 2D delamination remains uncertain and requires careful consideration.

Therefore, this research presents a comprehensive comparison of 1D and 2D delamination behaviours with different interface angles, with a focus on mode II-dominated delamination growth, using both experimental and numerical approaches. The mechanisms of mode II delamination growth were investigated through experiments, employing various testing techniques, including Digital Image Correlation (DIC), C-scan, and fractography, to monitor the delamination process and gain insights into the underlying damage mechanisms. The onset and evolution of different types of damage were also monitored by analysing the Acoustic Emission (AE) signals generated by the damage events. Based on the detection of delamination onset and propagation, the fracture toughness is decomposed by separating the total fracture toughness, G_{IIc}^{tot}, into intrinsic fracture resistance, $G_{IIc}^{intrinsic}$, and extrinsic toughening primarily caused by fibre bridging, $G_{IIc}^{extrinsic}$. A numerical scheme for simulating and comparing 1D and 2D delamination phenomena was validated by applying the decomposed fracture toughness through modified cohesive traction-separation laws. The comparison elucidates the similarities and discrepancies between 1D and 2D delamination behaviours, highlighting the importance of accurately determining fracture toughness by considering the dominant delamination mechanisms.

2. Experiment

2.1. Material system

A unidirectional carbon/epoxy composite prepreg, M30SC-DT120-200-36, was used to fabricate the UD and MD laminates through manual layup and autoclave curing, following the specifications provided in the technical data sheet [34]. The curing cycle involved heating to 120 °C at a rate of 2.4 °C/min, holding for 1.5 h, and cooling at the same rate. A cure pressure of 6.0 bar was applied throughout the curing cycle with a vacuum bag.

To investigate the influence of interface angles on mode II delamination behaviour, four different layups were designed for 1D tests, and two different layups were designed for 2D tests [20]. The specimen configurations are listed in Table 1. The MD layups for the 1D tests were specifically designed to mitigate the bending–torsion coupling effect on the mixed-mode ratio [35,36] and the geometric nonlinearity effect on the force–displacement response [37,38]. Initial delamination was introduced by embedding a thin Teflon sheet (0.016 mm thickness) at the middle interface. At least three specimens were tested for each of the 1D configurations, while one specimen was tested for each of the 2D configurations [20].

2.2. Test configurations and test procedure

The 1D experiments were conducted using the End-Loaded Split (ELS) test configuration, as recommended by the international standard ISO 15114 [39]. The ELS setup, shown in Fig. 2, provides more stable delamination growth under pure mode II loading compared to other test setups, such as ENF and 4-point bending [15,40]. The total specimen length (L_t) is 180 mm, while the effective length, including the clamped regions, (L_c) is 150 mm.

The test procedure followed the steps outlined below:

- Perform clamp correction tests to determine the effective flexural modulus.
- Conduct mode II pre-cracking tests with a loading rate of 0.5 mm/min (with a crack length of 5 to 10 mm).
- Perform mode II delamination tests with a loading rate of 0.5 mm /min.
- Determine the fracture toughness using the J-integral method [37] and the Corrected Beam Theory with Effective Crack Length (CBTE) [39].

In contrast to the 1D tests, a two-step testing procedure was used for the 2D Planar Central Loaded Split (PCLS) tests. The experimental setup is illustrated in Fig. 3. A pre-loading process was conducted to separate the Teflon sheet from the laminates without causing propagation. The formal tests were then performed following the pre-loading process, with a loading rate of 0.6 mm/min.

Table 1
Specimen configurations of 1D ELS tests and 2D PCLS tests.

Specimen	Initial interface	Layup	a_0	L	B	H=2h
UD(0//0)	0°//0°	$[0_{14}//0_{14}]$	52 ± 1	90	20.0 ± 0.1	4.54 ± 0.10
MD(0//0)	0°//0°	$[(0/0/90)_4/0_2//0_2/(0/0/90)_4]$	55 ± 1	90	20.0 ± 0.1	4.51 ± 0.05
MD(0//45)	0°//45°	$[(0/0/90)_4/0/45//0_2/(0/0/90)_4]$	55 ± 1	90	20.0 ± 0.1	4.45 ± 0.05
MD(0//90)	0°//90°	$[(0/0/90)_4/0/90//0_2/(0/0/90)_4]$	55 ± 1	90	20.0 ± 0.1	4.45 ± 0.05
PCLS(0//00)	0°//0°	$[0/90/45/-45]_s//[0/90/45/-45]_s$	9 ± 0.1	140	140	2.5 ± 0.05
PCLS(0//90)	0°//90°	$[0/90/45/-45]_s//[90/0/45/-45]_s$	9 ± 0.1	140	140	2.5 ± 0.05

$_s$ indicates a symmetrical layup, // indicates the interface with Teflon insert.

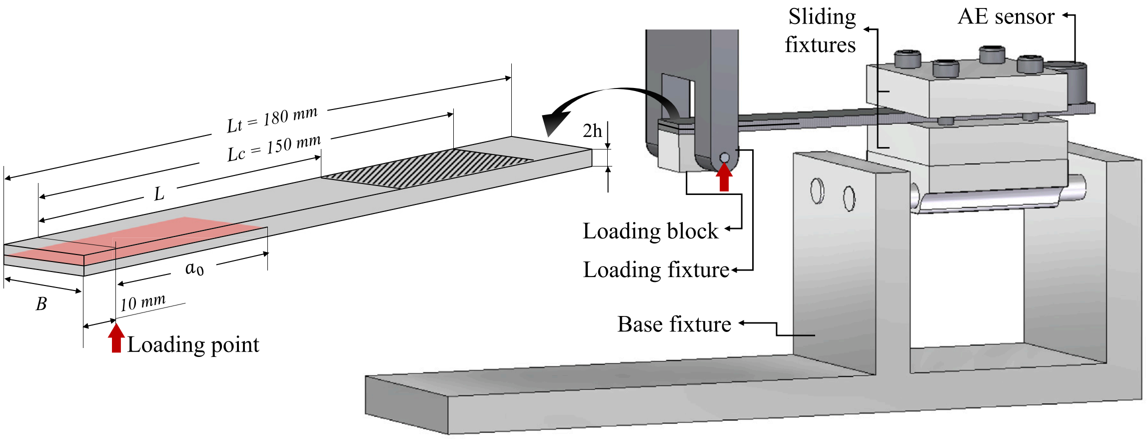

Fig. 2. Illustration of the ELS test setup. The specimen is fully clamped in the fixture, with 8 N m torque applied to each of the screws. The support frame is rigidly constrained to the base of the testing machine.

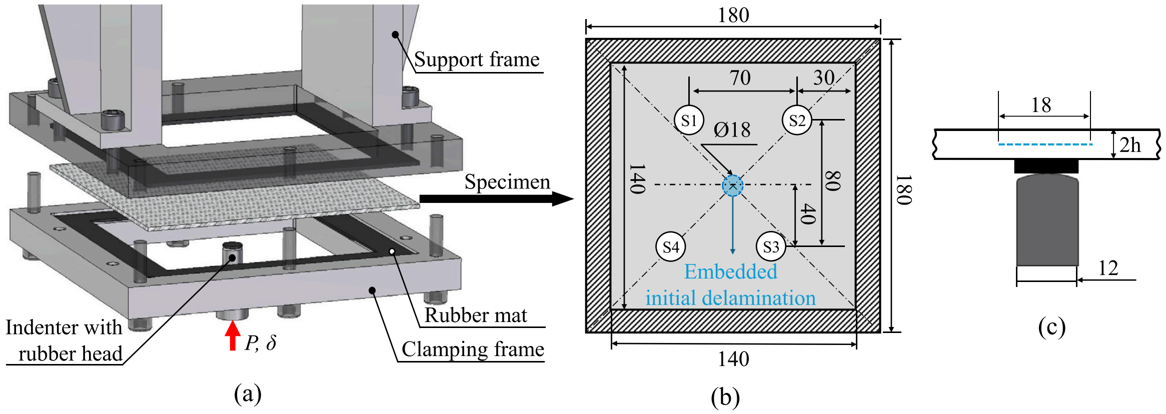

Fig. 3. Illustration of the PCLS test setup. The shaded region in the specimen configuration indicates the clamping area. (a) PCLS test fixtures, (b) top view of the specimen configuration, and (c) side view of the out-of-plane loading condition. Si (i = 1, 2, 3, 4) denotes the AE sensors. All measurements are reported in mm.

To monitor delamination growth, 3D DIC cameras were used to capture speckle images of the top surface throughout the loading process for both 1D and 2D experiments. The principal curvature from the DIC analysis is sensitive to delamination growth and was used to determine the 2D delamination contours [20]. For the 1D tests, an equivalent Strain Energy Density (SED) method based on DIC analysis (DIC-eSED) was used to track the delamination front [38]. The delamination growth measured from DIC analysis was compared with C-scan results.

Additionally, an AE system (Vallen Systeme) was used in both 1D and 2D tests to identify damage types and analyse their evolution. The sampling rate for the AE sensor (VS900-M) was 10 MHz. The thresholds for eliminating environmental noise were set at 38 dB for the 1D tests and 45 dB for the 2D tests, based on preliminary tests. The configurations of the AE sensors are shown in Figs. 2 and 3. For the ELS tests, the AE sensor was secured at the end of the specimen using a clamp. For the PCLS tests, the AE sensors were mounted at the designated locations using 3D-printed plastic holders, which were adhered to the specimens with glue. The rearm time and duration for transient signal acquisition were set to 400 μs, with a pre-trigger of 200 μs before recording each AE hit. This configuration provides a 1000-μs time window for capturing the AE transient signal wave. The AE features presented in Fig. 4 were extracted by analysing these signal waves.

Furthermore, clustering analysis was performed to separate different AE events, which can be correlated with different damage modes. The features for AE clustering were selected based on Principal Component Analysis (PCA) [41,42]. A cumulative contribution rate greater than 80% was considered, which was primarily composed of the first four principal components [43]. The first four AE features that contributed the most to the principal components were selected for the clustering analysis.

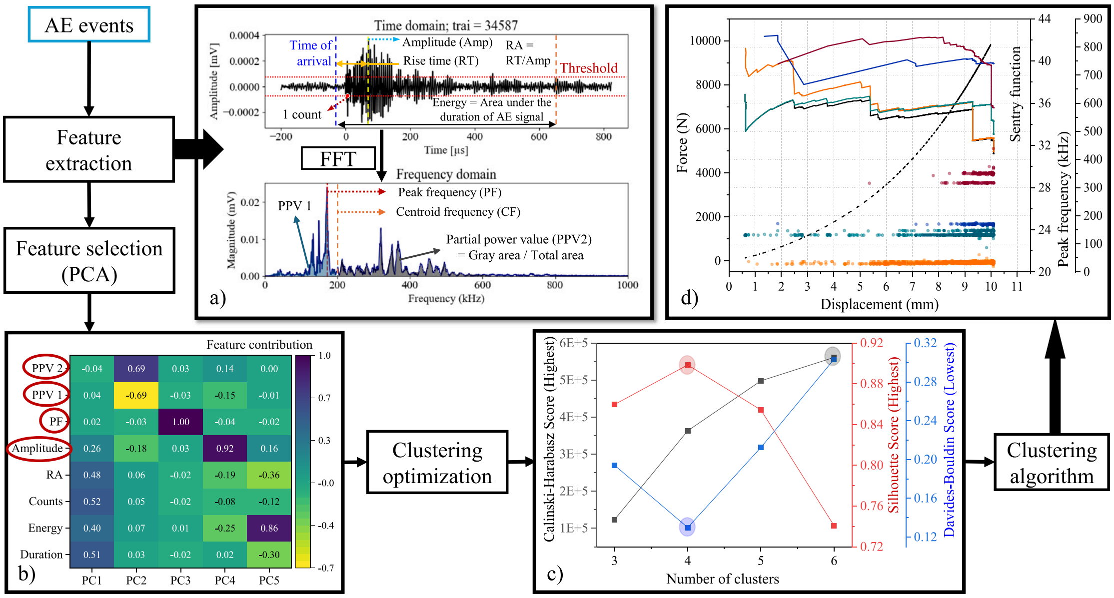

Fig. 4. Schematic of data processing and clustering analysis for the AE dataset: (a) extracted AE features in time and frequency domains; (b) feature selection based on PCA; (c) optimisation of the number of clusters; (d) clustering results.

A flowchart for AE clustering is illustrated in Fig. 4. The Partial Power Value (PPV) [44] was calculated as the ratio of the signal energy within specific frequency bands, obtained via Fast Fourier Transform (FFT) analysis in the frequency domain. The PPVs were used to characterise the energy distribution across low- and high-frequency bands. They capture variations in signal strength, especially where high-frequency components attenuate more rapidly than low-frequency components [44]. A centroid frequency of 200 kHz was used to separate the frequency range for the PPV calculation. The optimal number of clusters was determined by evaluating various validity indices, including the Calinski–Harabasz Score, Silhouette Score, and Davies–Bouldin Score (Fig. 4-c) [45,46]. Higher values of the first two scores and a lower value of the third indicate better clustering. The determination of cluster numbers also considered potential damage modes occurring during mode II delamination [38]. A hierarchical clustering algorithm was employed for the final clustering analysis, as it provides better reproducibility than K-means or Gaussian Mixture Model (GMM) when using the same PCA-selected features. A detailed comparison of the clustering algorithms is beyond the main scope of this study; comprehensive investigations can be found in Refs. [45–48].

Finally, to investigate the fracture surface morphology, fractographic observations of the delaminated surface were conducted using a 3D optical profilometer (Keyence VR-5000) and a Scanning Electron Microscope (SEM, JSM-7500F). Only the upper delamination surface (opposite the loading side) was selected for the fractographic analysis.

3. Numerical modelling

3.1. 1D and 2D models

A numerical investigation was performed using Abaqus2021 to simulate 1D and 2D delamination growth using the fracture toughness determined from the 1D experiments. An implicit/standard solver was utilised for quasi-static analysis. The numerical models for both 1D and 2D tests were constructed based on the experimental configurations shown in Figs. 2 and 3. The boundary conditions suggested in Ref. [49] were applied to the 1D model. For the 2D test, only a quarter of the square panel was modelled, utilising symmetry boundary conditions along the symmetry planes to improve computational efficiency.

Since the rubber mats in the clamping frame affect the boundary conditions, these components were also incorporated into the model to accurately represent the experimental loading and constraints. In the clamping region, the top surface of the upper rubber mat and the bottom surface of the lower mat were fully constrained to replicate experimental constraints. The rubber material properties were selected from Ref. [50], and its behaviour was simulated using a hyperelastic Yeoh model [51]. The coefficients for this model are provided in Table 2.

To enhance computational efficiency, the upper and lower sublaminates were each subdivided into three sections. As shown in Fig. 5, the middle two layers adjacent to the delamination interface were modelled with 3D solid elements using incompatible mode (C3D8I) to accurately capture the stress states at the interface. The remaining layers were represented by continuum shell elements (SC8R), assigned with a section property that replicates the composite layup provided in Table 1. Reduced integration was applied to mitigate shear locking, with enhanced hourglass control included to prevent severe element distortion. Frictionless hard contact is applied to the interfaces to prevent surface penetration.

A cohesive zone model (CZM) was used to simulate delamination at the interfaces of interest. The interfaces were represented by 8-node 3D cohesive elements (COH3D8). For the 2D model, CZM was employed not only to simulate the delamination interface but also to capture intralaminar cracks responsible for delamination migration (Fig. 5(e)). The material properties of the CFRP composites used in both models are summarised in Table 3. A sensitivity analysis of the estimated material properties confirmed that reasonable variations in $\nu_{12} = \nu_{13}$ (0.25~0.30), ν_{23} (0.30~0.40), and G_{23} (3000~4000 MPa) present no significant influence on the force–displacement response, the local stress state, or the progression of delamination.

3.2. Cohesive law for mode II delamination growth

A multi-point cohesive constitutive model is proposed based on the decomposition of G_{IIc}^{tot} to describe the mode II delamination process [38,53–55]. The cohesive constitutive model, along with the damage onset and evolution criteria, are provided in Appendix. As shown in Fig. 5(c), several control parameters are defined in the cohesive model to determine the damage stage during the stiffness degradation process. The corresponding traction levels of these points are determined by scaling the matrix tensile strength Y_T with coefficients a to d. Another

Table 2
Material coefficients of Yeoh model in Abaqus [50].

C_{10} (MPa)	C_{20} (MPa)	C_{30} (MPa)	D_1	D_2	D_3	R^2
0.2019	4.43×10^{-5}	1.30×10^{-4}	2.18×10^{-3}	8.68×10^{-5}	-1.79×10^{-5}	0.9962

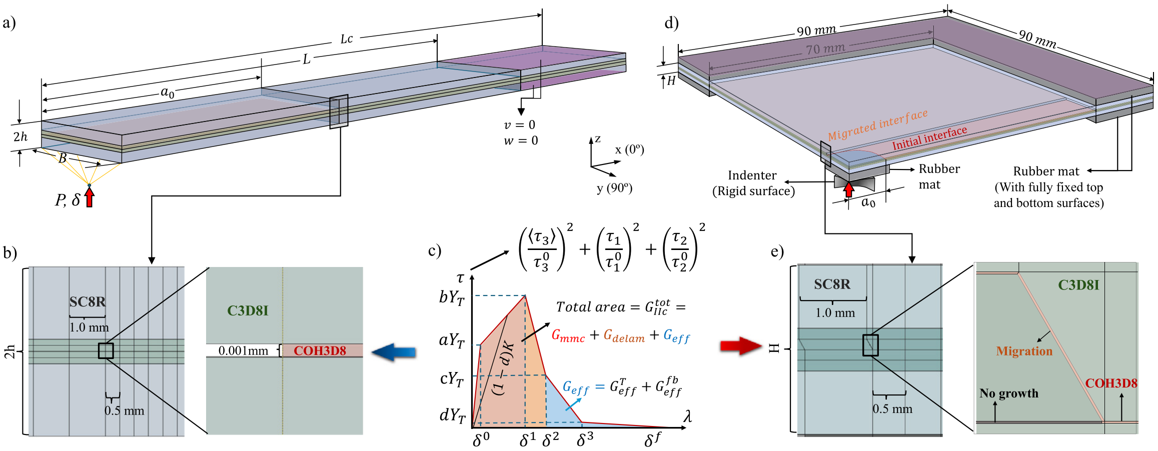

Fig. 5. Finite element models for (a) ELS specimen, and (d) PCLS specimen. The element types and locations of cohesive elements are detailed in (b) for the 1D model and (e) for the 2D model. The modified cohesive constitutive model, implemented in the simulations, is depicted in (c).

Table 3
Engineering constants of the DT120 carbon/epoxy prepreg [34].

Properties	Test method	Value
Tensile Modulus (0°) E_{11} (GPa)	ASTM D3039	145.0
Tensile Modulus (90°) $E_{22} = E_{33}$ (GPa)	ASTM D3039	6.4
Tensile Modulus (90°) $E_{22} = E_{33}$ (GPa)	ASTM D3039	6.4
In-plane shear Modulus $G_{12} = G_{13}$ (GPa)	EN 6031	3.38
Transverse shear Modulus G_{23} (GPa)	–	3.92[a]
Tensile Strength (0°) X_T (MPa)	ASTM D3039	3010
Tensile Strength (90°) Y_T (MPa)	ASTM D3039	39
In-plane Shear Strength $S_{12} = S_{13}$ (MPa)	EN 6031	95.6
ILSS (MPa)	EN 6031	77.2
Poisson's ratio $v_{12} = v_{13}$	–	0.26[a]
Poisson's ratio v_{23}	–	0.31[a]
Mode I fracture toughness G_{Ic} (kJ/m^2)	ASTM D5528-01	0.219 [52]

[a] indicates an estimated value

control parameter γ is used to separate the $G_{IIc}^{extrinsic}$ into an effective toughening $G_{eff}^T = \gamma G_{eff}$ due to the development of fibre bridging zone, and energy dissipation G_{eff}^{fb} due to fibre breakage. The modified cohesive model was implemented using a User Material (UMAT) subroutine.

An optimal set of parameters provides a precise estimation of the traction distribution at the crack front [56]. Researchers have made efforts to correlate the cohesive parameters with the mechanical properties of composite laminates [21,57,58]. However, the selection of penalty stiffness K and critical traction τ varies across the literature [59]. The matrix tensile strength was used as the critical traction in Ref. [53] for mode I delamination. Meanwhile, it is suggested in Ref. [21] to use normal and shear traction values equal to 55%–65%, 50%–60% and 50%–75% of the matrix tensile strength Y_T. These parameters are highly dependent on the model geometry, element size, and loading and boundary conditions.

A comprehensive investigation into the selection of optimal cohesive parameters has been conducted by Turon et al. [56], who proposed a correlation between normal and shear traction values expressed as $\tau_{sh}^0 = \tau_n^0\sqrt{G_{IIc}/G_{Ic}}$ for mixed-mode cohesive model. The cohesive parameters, together with the element size, have influence on the virtual FPZ and therefore affect the delamination process. This interplay complicates the determination of an appropriate set of parameters for different material systems or test setups. In general, a lower τ can provide better convergence, but a very low τ value may result in an inaccurate force–displacement response [58].

Since there is no consistency in the cohesive parameters, the parameters in the modified cohesive model were determined through trial and error until a satisfactory match between the numerical results and experimental data was achieved. A constant penalty stiffness of $K = 1 \times 10^5$ MPa/mm was used for all analyses, as suggested in Ref. [18]. In addition, the default bilinear cohesive law was applied to the intralaminar cohesive elements (migration), with the critical traction set to the matrix tensile strength Y_T, and a fracture toughness corresponding to mode I G_{Ic} [52].

A mesh sensitivity test was conducted using a characteristic cohesive element length ranging from 0.1 mm to 2.0 mm. An optimal element length of 0.5 mm was selected for all simulations to balance accuracy and computational efficiency. The element size in the regions outside the cohesive zone was increased to 1 mm for the 1D model and 2.5 mm for the 2D model. The numerical results obtained using the modified cohesive model (indicated by 'UMAT') were compared with the default Bilinear model (indicated by 'Bi').

3.3. Calibrated cohesive models

As previously mentioned, the parameters of the modified cohesive model were calibrated through a trial-and-error approach, by minimising the discrepancy between numerical predictions and experimental results. In this case, the calibrated model is suitable for investigating the influence of model parameters on delamination behaviour, rather than for predicting delamination growth in real-world applications.

The procedure for calibrating the cohesive models used to simulate 1D and 2D delamination growth is illustrated in Fig. 6. First, the modified multi-point cohesive model (UMAT) is numerically calibrated by tuning the cohesive parameters to achieve better agreement with experimental results, compared to the bilinear cohesive models. The calibrated model (UMAT(1D)) is then applied to predict 2D delamination growth. Based on comparisons between the simulation and experimental results, the multi-point model is either adopted directly for 2D simulations or further calibrated using the 2D experimental data. Then, the performance of the recalibrated cohesive model (UMAT(2D)) is compared with the bilinear models.

It is important to note that, for 1D calibration, the total fracture toughness G_{IIc}^{tot} is specified for each specimen configuration. However,

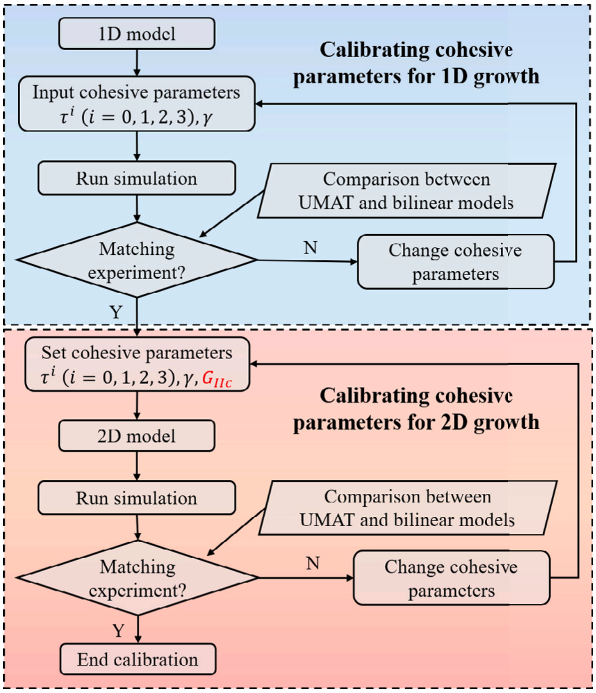

Fig. 6. Procedure for calibrating cohesive models for simulation of 1D and 2D delamination growth. The calibrated parameters from 1D simulation are used as initial values for simulating 2D delamination growth, to assess whether the model calibrated from 1D tests is sufficient for capturing 2D behaviour. If discrepancies arise, G_{IIc} is then considered as a variable in 2D simulation.

for 2D delamination growth, the extrinsic toughening mechanisms may differ from those observed in 1D. Therefore, the extrinsic component of the fracture toughness is treated as a variable, adjustable based on 2D experimental results, whereas the intrinsic component is considered a constant that depends only on the interface angle.

The calibrated cohesive models are presented in Fig. 7, alongside the default bilinear models (indicated by 'Bi') for comparison. The calibration was achieved by tuning the cohesive parameters to precisely replicate the force–displacement response and delamination growth trends. The decomposed values of G were obtained experimentally. The control parameters $\tau_i (i = 0, 1, 2, 3)$ were calibrated via a brute-force search over possible combinations of traction values. Initially, τ_0 was fixed using Y_T, τ_1 was set to the interlaminar shear strength (ILSS) by default, and τ_2 corresponded to the bridging-related traction [18]. Finally, τ_3, representing the tail of the traction–separation curve, was numerically adjusted until a satisfactory match with the delamination growth curves was achieved.

For 1D ELS model, the multiple traction values are tuned based on the transverse tensile strength Y_T of the lamina using scaling factors $a \sim d$. As shown in Fig. 7, the cohesive models present differences between the $0°//0°$ interface and the angled interfaces $0°//\theta°$ $(\theta > 0°)$. Notably, although the shape of cohesive model remains the same for 1D $0°//0°$ interfaces (UD and MD(0//0) specimens) or angled interfaces (MD(0//45) and MD(0//90) specimens), the area of the coloured regions varies, depending on the decomposition of fracture toughness (Fig. 9). Bilinear models with identical total fracture toughness G_{IIc}^{tot} but different critical traction τ^0 and τ^1 were used to investigate the influence of the critical traction on the simulation of 1D delamination growth.

The modified cohesive model for the 2D $0°//0°$ interface (coloured region in Fig. 7-c) is specifically calibrated to simulate delamination growth at the initial interface of the PCLS(0//0) specimen. For the migrated interface in the PCLS(0//0) specimen, as well as both the initial and migrated interfaces in the PCLS(0//90) specimen — all of which are $0°/90°$ interfaces — the same cohesive model is applied (coloured region in Fig. 7-d).

In addition, bilinear cohesive models were also implemented to simulate 2D delamination growth, aiming to evaluate their effectiveness in predicting planar delamination using either the total fracture toughness G_{IIc}^{tot} or intrinsic fracture toughness $G_{IIc}^{intrinsic}$, with critical traction $\tau^0 = Y_T$ (represented by navy blue or dashed light blue lines in Fig. 7-c and 7-d).

In order to validate the numerical modelling approach, the force–displacement response and the flexural deformation at the top surface were compared between the numerical and experimental results. As presented in Fig. 8, the out-of-plane deflection along the central line at the top surface was extracted for both 1D (ELS) and 2D (PCLS) models. The modelling strategy presented in Fig. 5 demonstrates proper match with the experimental results obtained from the DIC analysis. For the 2D model, modelling the rubber mats at the clamping area accurately described the boundary conditions.

4. Experimental and numerical results

4.1. 1D results

As recommended by the ISO standard [39], the fracture toughness was calculated using the CBTE method, which includes a correction for the FPZ and a clamping condition correction. The R-curves are shown in Fig. 9. The total energy release rate (ERR), G_{IIc}^{tot}, calculated using CBTE, exceeds the ERR obtained from the J-integral, which excludes extrinsic toughening mechanisms such as fibre bridging and interface friction [37]. The left end of the R-curves corresponds to the onset of delamination growth, as detected by AE.

The total ERR G_{IIc}^{tot}, the intrinsic ERR at the onset point J^{init}, and the intrinsic ERR during the stable propagation phase J^{prop} were extracted from the R-curves and summarised in Fig. 9b. For MD specimens, the interface angles of the MD specimens show a negligible influence on G_{IIc}^{tot} and J^{prop}. The slight differences in G_{IIc}^{tot} can be attributed to variations in fibre bridging intensity across different specimens. The UD specimen exhibits the highest ERR values compared to the MD specimens, ascribed to intensive fibre nesting and bridging at the interface (Fig. 12). The values of G_{IIc}^{tot} and J^{prop} are comparable with those obtained from Ref. [38] for the same material system but different laminate layups. The MDs specimens follow the same stacking sequence as the PCLS specimens, while the UDs specimen contains fewer layers (16) compared to the 28 layers in the present UD configuration. The differences observed between specimens with the same interfaces can be attributed to variations in the stacking sequence and overall specimen stiffness, which influence the development of FPZ and fibre bridging zone [60].

The comparison of ERRs between MD and MDs specimens indicates that specimen stiffness also affects ERR calculation. In the more compliant MDs specimens, geometric nonlinearity complicates J-integral evaluation and total ERR determination, leading to greater scatter and reduced accuracy. Therefore, ERRs derived from the MD and UD specimens were used for numerical simulations of both 1D and 2D delamination behaviours, where the predicted force–displacement response and delamination growth were compared against experimental results.

The force–displacement responses and delamination growth curves from the ELS tests and simulations are shown in Fig. 10. The numerical force–displacement response and propagation curves from the modified cohesive law (red curves) are compared with the experimental results (black curves). The bilinear cohesive model with varying critical traction values produces comparable results (blue curves). The simulation results using different cohesive models closely align during the initial linear phase. For the bilinear cohesive model, a higher critical traction $(\tau^1 = 78$ MPa) produces a higher peak force followed by a rapid

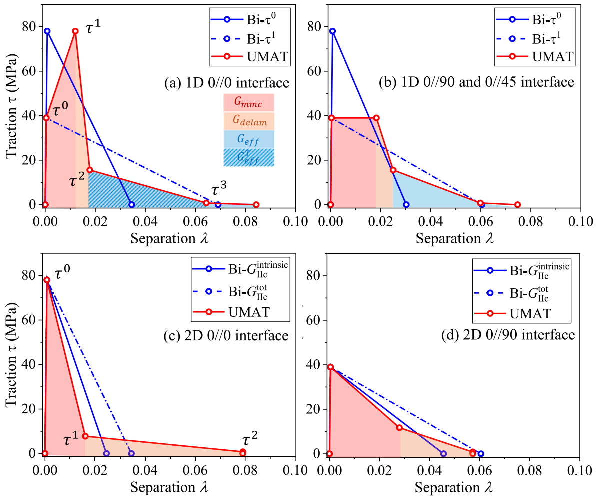

Specimen	$\tau^0 = aY_T$	$\tau^1 = bY_T$	$\tau^2 = cY_T$	$\tau^3 = dY_T$	$G^T_{eff} = \gamma G_{eff}$
	a	b	c	d	γ
UD(0//0)	1.0	2.0	0.4	0.02	0.98
MD(0//0)	1.0	2.0	0.4	0.02	0.98
MD(0//45)	1.0	1.0	0.4	0.02	0.98
MD(0//90)	1.0	1.0	0.4	0.02	0.98
PCLS(0//0)	2.0	0.2	0.02	0	0
PCLS(0//90)	1.0	0.3	0.02	0	0

Fig. 7. Comparison of the modified cohesive models (UMAT) with the default bilinear models. The calibrated cohesive parameters for all specimens are summarised in the table.

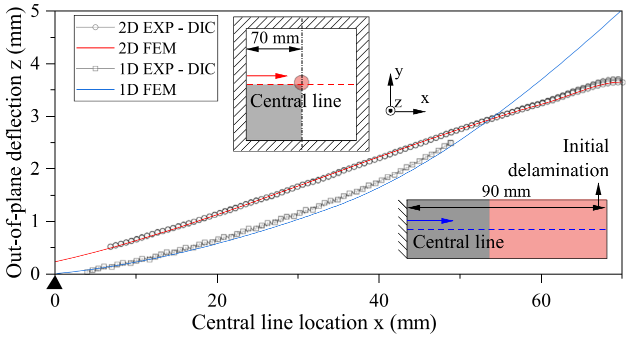

Fig. 8. Comparison of out-of-plane deflection between DIC measurement and numerical results. The blue curve represents the numerical result from the 1D simulation, while the red curve represents the result from the 2D simulation. (For interpretation of the references to colour in this figure legend, the reader is referred to the web version of this article.)

decrease in the force response once delamination propagates, whereas a lower critical traction ($\tau^0 = 39$ MPa) results in a more gradual reduction in the reaction force. The modified cohesive model yields numerical results that lie between the stiffer and softer responses predicted by the bilinear model. Overall, the choice of cohesive model has only a minor influence on both the force–displacement response and delamination growth trends. Across all specimens, the numerical results closely match the experimental data during the initial linear stage. For the MD specimens, the numerical results are slightly higher than the experimental measurements, likely due to the testing frame compliance, which has a more pronounced influence for the relatively compliant MD specimens. The influence of different cohesive constitutive models on 1D delamination behaviour is further discussed in Section 4.4.

For experimental results, compared to the 0°//0° interface, the 0°//45° and 0°//90° interfaces exhibit a more gradual force reduction, reflecting slower and more stable delamination growth. The delamination area was measured using the DIC-eSED method developed in Ref. [38]. The progressive delamination areas are shown in Fig. 11. The delamination contours captured using the DIC-eSED method are irregular and vary in shape as propagation progresses. At the 0°//45° interface, a slightly tilted delamination front is observed. Consequently, delamination area, rather than side length, is measured to provide a more representative description of the actual growth and to construct the fracture resistance curve (R-curve).

Fractographic analysis was then performed to investigate the damage modes governing the delamination process. As shown in Fig. 12, the surface fracture morphologies obtained from SEM reveal distinct damage modes at different interfaces. Small matrix cracks (cusps) formed and propagated due to shear stress at the interfaces. These cracks coalesced under increasing load, leading to a fully delaminated interface. This behaviour was observed across various specimen interfaces. In MD specimens with 0°//45° and 0°//90° interfaces, large-area matrix cracking was observed, oriented along the angled fibre orientation. This can be attributed to the resin-rich regions at the interfaces. Large-scale fibre bridging is evident in all specimens, covering the entire delaminated area. However, the intensity of bridging fibres and the bridging angles varied among specimens (Fig. 12). In the UD specimen, the delamination surface exhibited greater height variations than in the MD(0//0) specimen, indicating more pronounced fibre nesting. As a result, the interface was less clearly defined, allowing matrix cracks to propagate into the nested fibres and thereby promoting fibre–matrix debonding and fibre bridging.

Although different interfaces exhibit distinct fractographic morphologies, similar damage modes are observed across specimens. Experimental observations identified three characteristic damage mechanisms: matrix cracking (small or large cusps), fibre–matrix debonding (associated with delamination), and fibre breakage. The onset and evolution of these damage modes were further analysed through AE clustering.

4.2. 2D results

In 2D PCLS experiments, the propagation of an initially embedded circular delamination was monitored using DIC and C-scan techniques. As shown in Fig. 13, the embedded circular delamination propagated along the 0° fibre orientation at the initial interface (deep orange), but migrated to another interface where the normal direction of the circular front became perpendicular to the 0° layer. The migrated delamination then propagated along the 90° fibre orientation (light orange). For the PCLS(0//0) specimen, the delamination contour captured by C-scan, including regions near the top surface (blue area, Fig. 13), is well reflected in the surface curvature contours. Overall, the DIC contour closely matches the C-scan results at maximum deflection. For the PCLS(0//90) specimen, the maximum vertical and horizontal dimensions of the delamination area also closely agree with the C-scan measurements.

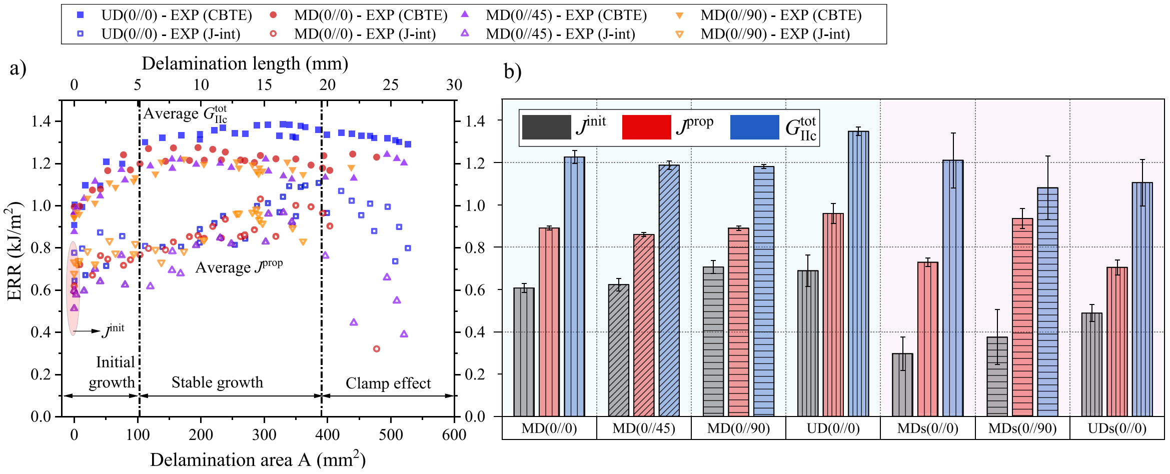

Fig. 9. (a) Experimental R-curves and (b) a summary of decomposed ERRs based on onset and propagation ERR values extracted using the compliance and J-integral methods. ‘s’ denotes the experimental results obtained using specimens with quasi-isotropic layups from Ref. [38].

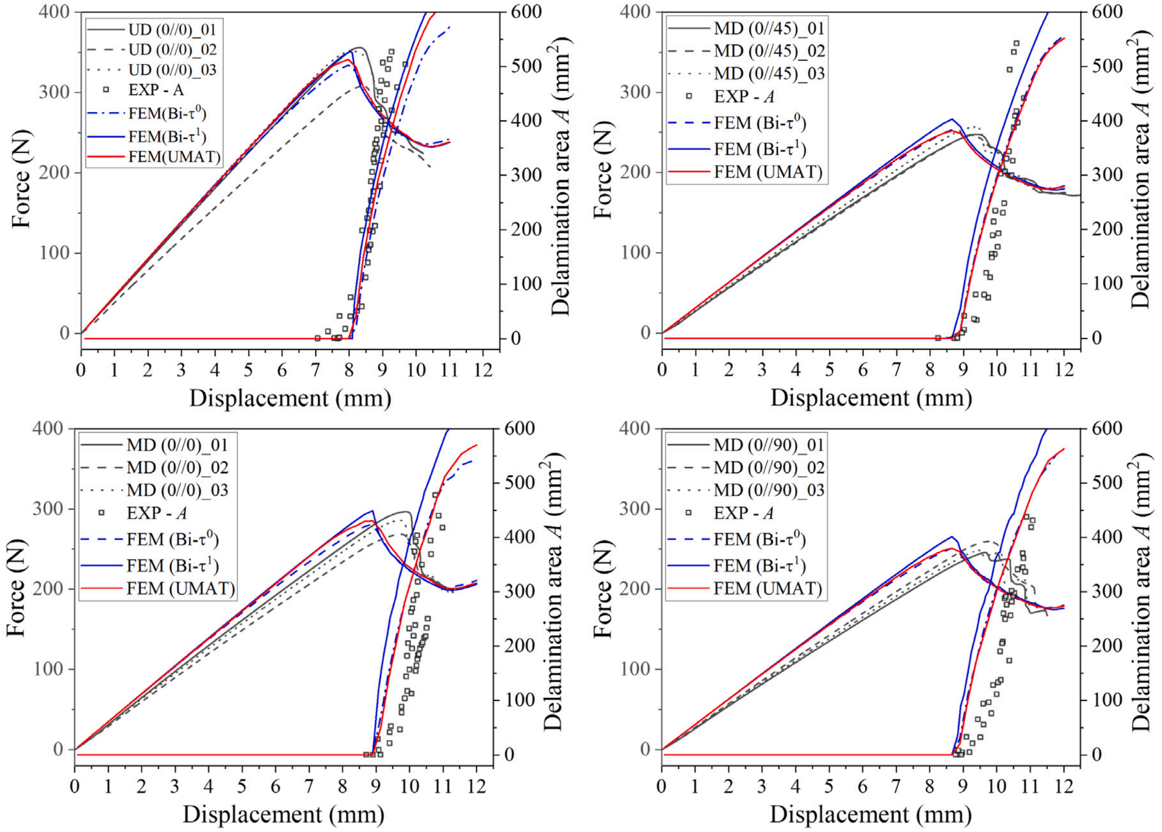

Fig. 10. Force and delamination area versus displacement curves for 1D ELS specimens. ‘EXP’ denotes the experimental results, while ‘FEM’ represents the numerical results from the finite element model.

The delamination lengths a_{init} and a_{mig}, measured by the maximum dimensions of the delamination area from the DIC curvature and C-scan, were compared with the numerical results. As shown in Figs. 14 and 15, a quarter of the specimen is used for comparing the test results with the simulated delamination growth. Initially, the cohesive model calibrated from 1D tests was used to predict planar delamination growth. The results (grey dashed contour) are almost identical to those obtained using the bilinear cohesive model with the total fracture toughness G_{IIc}^{tot} (dark blue dashed contour). These contours lie within the DIC-estimated delamination contour, indicating that the numerical model underpredicts planar delamination growth when using the total fracture toughness G_{IIc}^{tot} obtained from 1D experiments. In contrast, using the intrinsic fracture toughness J^{prop} slightly overpredicts delamination growth (light blue dashed curves). The modified 2D cohesive models show a good agreement with the DIC measurements of delamination growth in both the vertical and horizontal directions.

Compared to the C-scan results at the highest deflection, the numerical model overpredicts delamination growth in the diagonal direction. This discrepancy arises because intralaminar damage was not considered in the numerical model. It is important to note that the cohesive law does not account for mode mixity, as delamination growth along the fibre orientation is primarily driven by mode II. The displacement

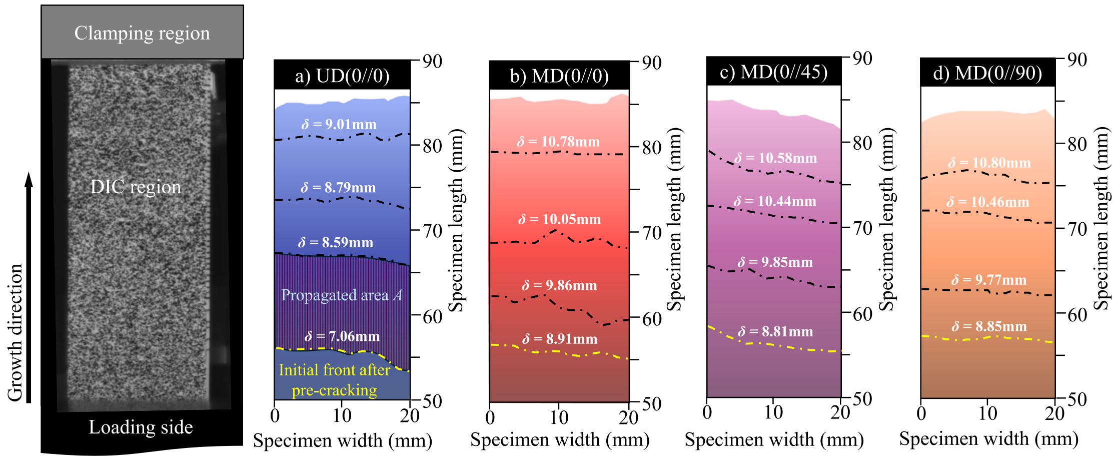

Fig. 11. Variations in the delamination front captured by the DIC-eSED method during testing [38]. The shaded regions represent C-scan results obtained after the tests. Delamination area A was captured by the area between the current delamination front and the initial front after pre-cracking.

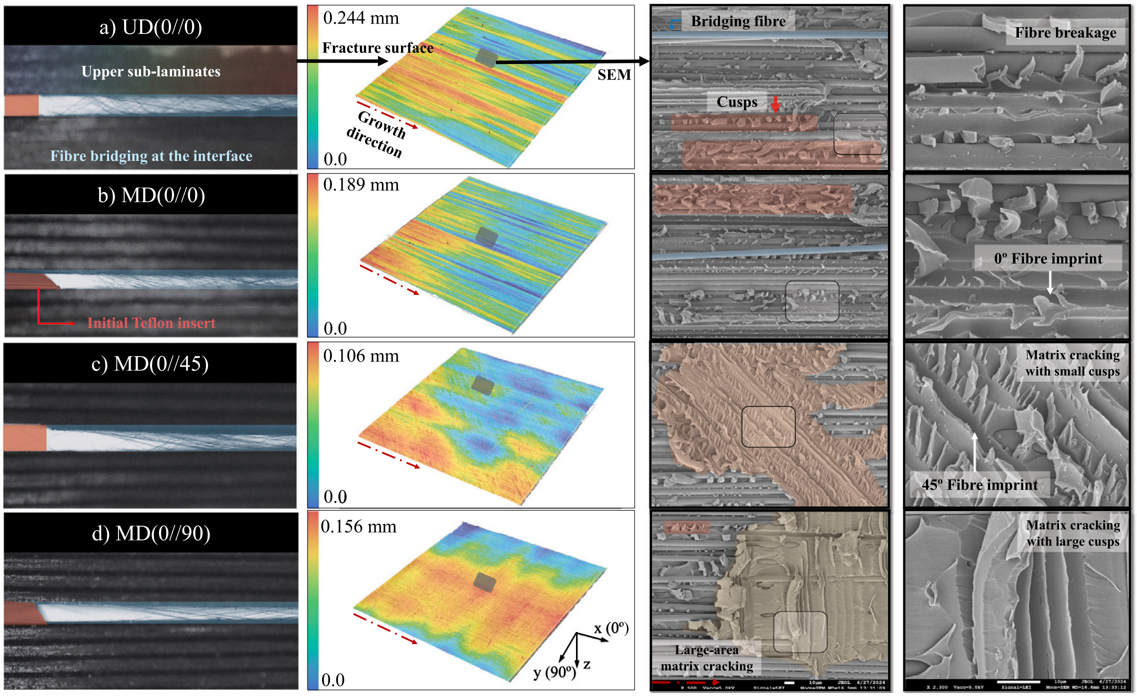

Fig. 12. SEM observation at the upper fracture surface for ELS specimens with different interfaces. The colour bar in the second column indicates the height distribution. fibre bridging, shown in the left column, was observed using an optical microscope under 3 mm opening displacement.

jump, λ (in Eq. (2)), is normalised by shear splitting in the fibre direction δ_1 (local mode II), and transverse to the fibre direction, δ_2 (local mode III). The normalisation of the displacement jump with both δ_1 and δ_2 results in larger shear splitting, which induces more delamination growth compared to C-scan results. In reality, local mode III does not induce delamination growth but rather intralaminar cracking. As delamination propagates, it may migrate to another critical interface, which is not accounted for in the current numerical model. Consequently, delamination growth along the diagonal direction is less in the experiments than in the simulations, due to the interaction between matrix cracking through the ply and interfacial delamination under local mixed-mode II/III [20].

Fig. 16 presents a comparison between the force–deflection curves and propagation curves obtained from experiments and simulations. The force–deflection curves show good agreement with the experimental results. Using the maximum length at the initial and migrated interfaces, the delamination growth curves from the modified cohesive model (red solid curves) closely match the experimental data (scatter plots). However, a larger discrepancy is observed when considering the total delamination area. This deviation can be attributed to measurement errors in the diagonal direction when capturing delamination growth using DIC, as illustrated in Fig. 13. Notably, the delamination area curves show a better agreement with the C-scan results. In contrast, the default bilinear cohesive law results in either overestimation or underestimation of delamination growth when using the total ERR G_{IIc}^{tot} or the intrinsic ERR J^{prop}, respectively.

According to the force–deflection response, no significant stiffness reduction was observed due to delamination growth. Force increases exponentially with displacement, attributed to geometric nonlinearity (in-plane stretching) [18] and material nonlinearity (strain-dependent stiffening) [61]. Experiments were terminated upon severe flexural fracture. Numerical force–deflection curves are similarly unaffected by delamination growth, regardless of the cohesive model; therefore, only one set of simulation results is presented.

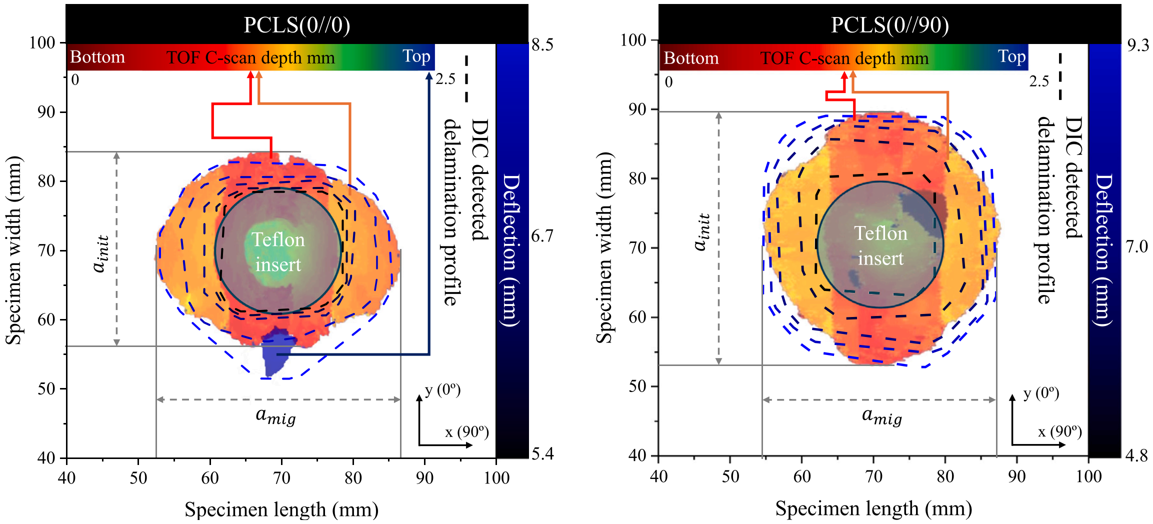

Fig. 13. Advancing delamination contours detected using the surface curvature in 2D PCLS specimens. The colour bars indicates the interface depth obtained from C-scan and the out-of-plane deflection level measured by DIC, respectively.

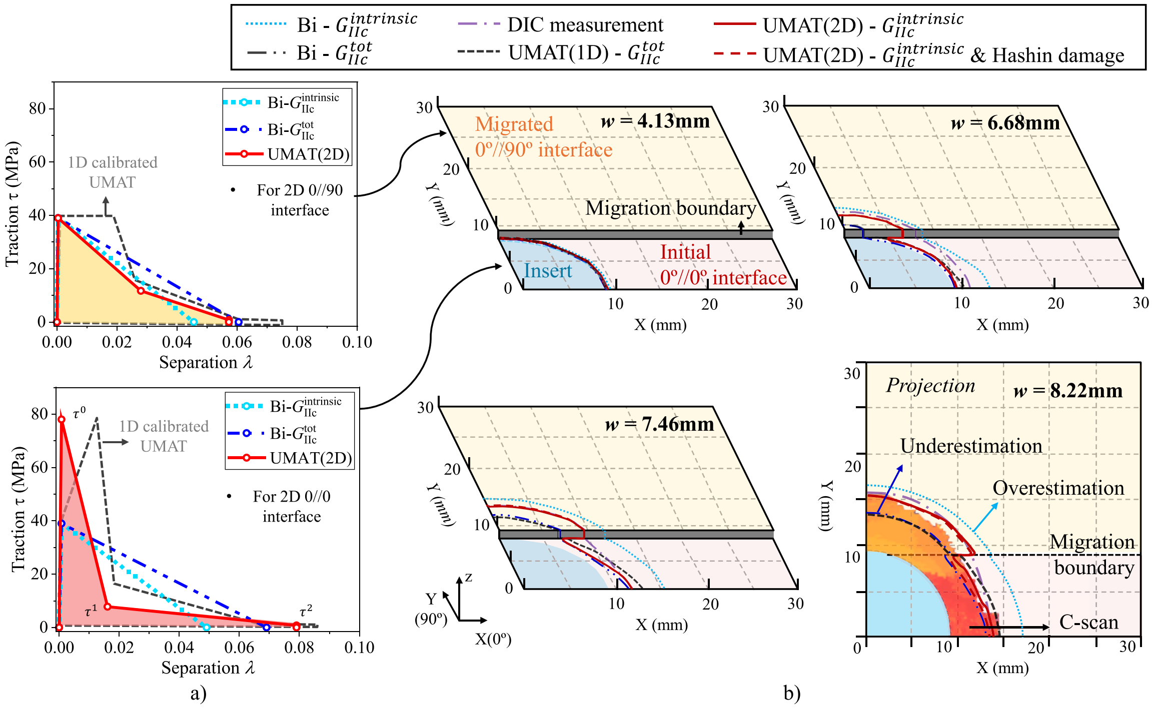

Fig. 14. (a) Cohesive models applied in simulations of the PCLS(0//0) specimen. (b) Comparison of delamination growth captured by DIC and C-scan, alongside simulation results using different cohesive models. The background colour represents the 0°//0° interface (red) and 0°//90° interface (yellow), with corresponding cohesive models shown in (a). (For interpretation of the references to colour in this figure legend, the reader is referred to the web version of this article.)

To predict flexural failure and assess its impact on delamination behaviour, the 2D Hashin damage criterion is activated in the SC8R shell elements. Using the modified 2D cohesive model, delamination growth predicted with and without Hashin damage criterion shows no significant difference, as indicated by the delamination contours represented by red dashed and solid lines in the first three steps of Fig. 14b. This is because the flexural failure has not developed sufficiently to cause a significant reduction in stiffness. For PCLS(0//90), when critical flexural failure occurs, delamination propagation slows down. Since delamination growth is not substantially affected by damage evolution in the sublaminates before the onset of critical flexural failure, the prediction results without activating the 2D Hashin damage criterion can be used for comparison with the experimental results.

It is worth mentioning that the calibrated cohesive model for 2D delamination growth is dependent on a single specimen result and is therefore not a general solution for prediction of delamination growth in other test configurations. The tuning of the cohesive parameters is empirical and dependent on the test configurations. The modified cohesive model is only used to provide flexibility for conducting a parametric study on the influence of the cohesive model shape on the 1D and 2D delamination behaviours. The 2D experiments in this study primarily serve as an initial validation of the proposed numerical

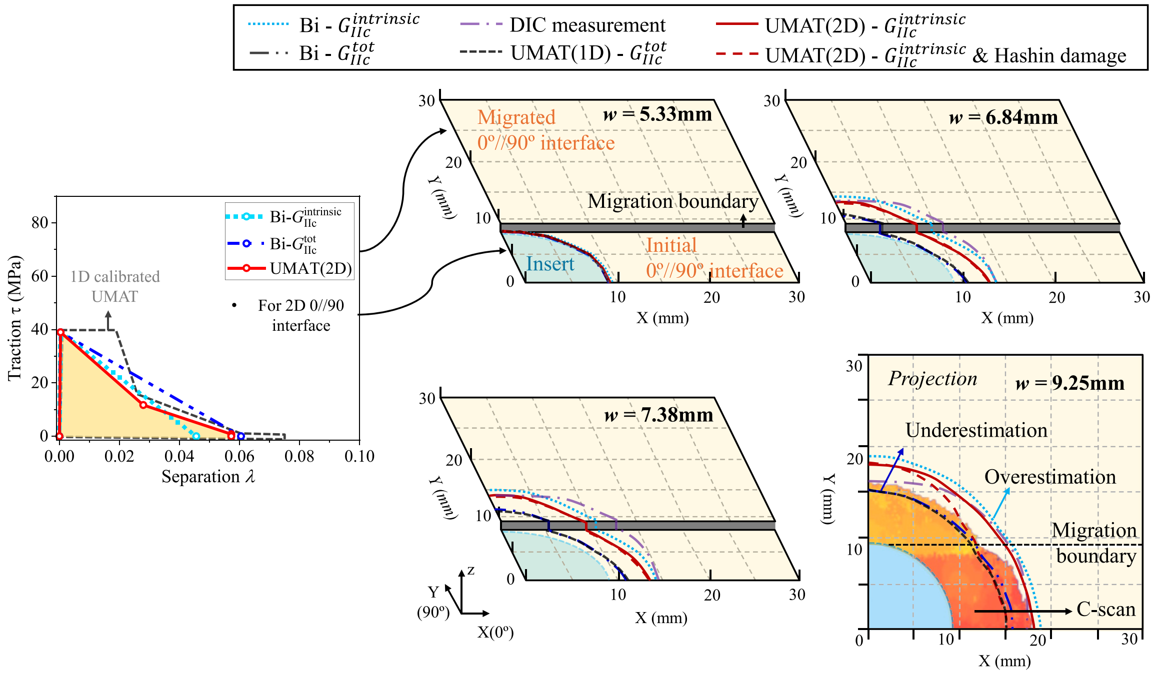

a) b)

Fig. 15. (a) Cohesive models applied in simulations of the PCLS(0//90) specimen. (b) Comparison of delamination growth captured by DIC and C-scan, alongside simulation results using different cohesive models.

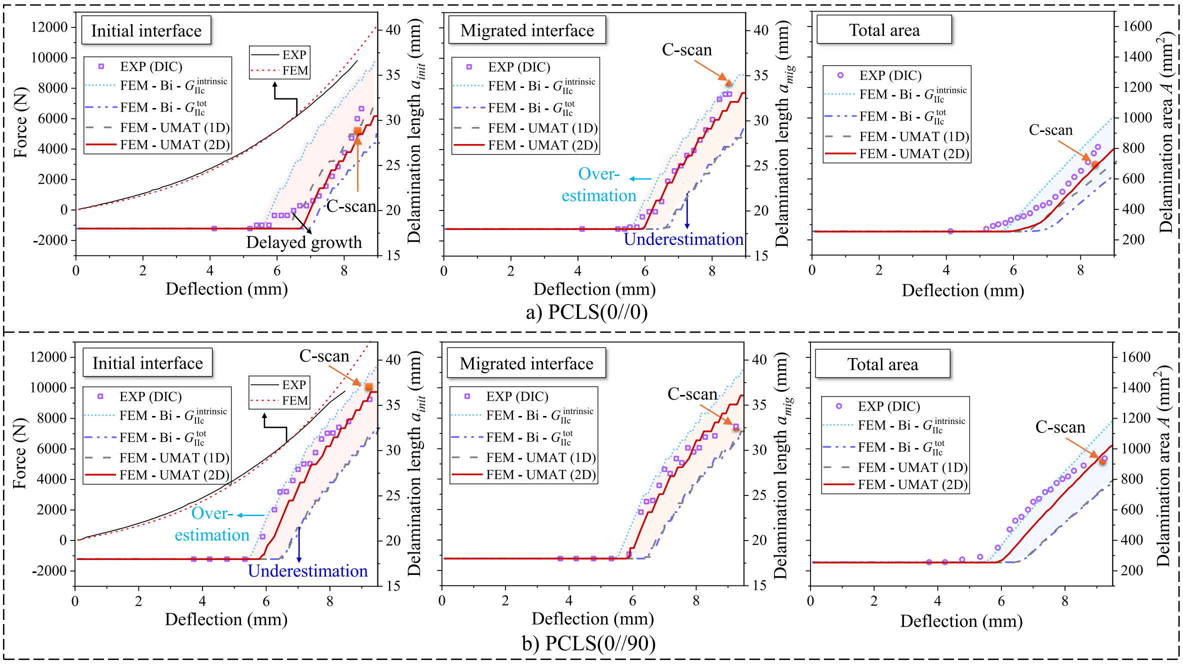

a) PCLS(0//0)

b) PCLS(0//90)

Fig. 16. Reaction force and delamination growth versus deflection curves for PCLS specimens. The deflection is determined at the central point of the upper surface using DIC. The measurements of the delamination area (A), initial interface delamination length (a_{init}), and migrated interface delamination length (a_{mig}) are illustrated in Fig. 14. Comparison between simulation results using different cohesive models are illustrated using lines with 'FEM' initial in the legends.

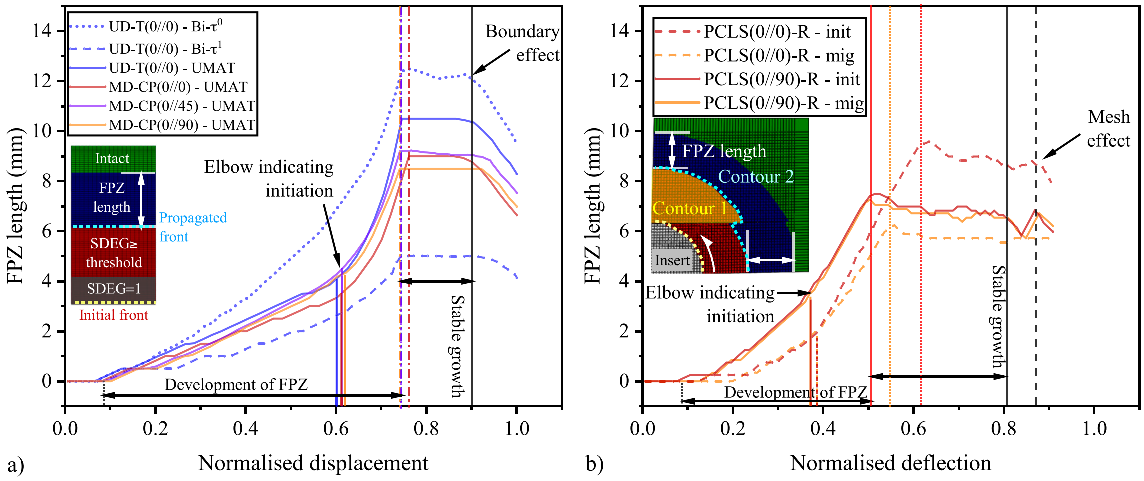

Fig. 17. Development of virtual FPZ extracted from numerical results for (a) 1D delamination growth and (b) 2D delamination growth. Numerical results from different cohesive models were compared for ELS UD specimens, while FPZ evolution in PCLS specimens was predicted using only the modified cohesive model. In the numerical plots, red indicates delamination with fibre bridging (SDEG above threshold), grey shows complete interface failure (SDEG = 1), and blue represents the virtual FPZ (SDEG between 0 and the threshold). (For interpretation of the references to colour in this figure legend, the reader is referred to the web version of this article.)

approach, rather than as a statistically representative characterisation of planar delamination behaviour. Their main purpose is to demonstrate the feasibility of the modelling framework and to highlight the limitations of directly transferring 1D fracture toughness measurements to more complex 2D delamination scenarios.

4.3. Damage evolution in 1D and 2D growth by CZM

The difference between the bilinear and modified cohesive models is analysed through the virtual FPZ. As shown in Fig. 17, the numerically predicted delamination area is divided into three regions. The red area represents the delaminated region with developing fibre bridging, where the damage variable (SDEG) exceeds the damage threshold. This threshold corresponds to the damage value when the traction reduces to control point τ_3. The grey area indicates complete interface failure (SDEG = 1). The blue area represents the virtual FPZ, where SDEG varies between 0 and the threshold, capturing the progressive damage accumulation before full delamination occurs.

For ELS specimens, cohesive damage initiates early in the loading process, accompanied by an increasing virtual FPZ length. This can be correlated to the onset of the micro matrix cracks along the crack tip that form the cusps. As displacement increases, the FPZ length continues to grow. Using the modified cohesive models, a distinct transition in the slope of the FPZ curves is observed. This “elbow” point marks the onset of delamination growth when the second control point τ_2 is reached, triggering a rapid traction drop and accelerated stiffness degradation. In contrast, the bilinear cohesive model fails to capture this transition point. The virtual FPZ length eventually reaches a plateau. This signifies stable delamination growth, occurring when the SDEG reaches the threshold at τ_3. Total failure of the cohesive elements follows when the SDEG reaches 1. The subsequent decrease in FPZ length is attributed to boundary effects, as delamination propagates closer to the clamping side, where interlaminar shearing becomes restricted.

Similar to 1D growth, the onset and stable delamination growth phases can be identified in 2D cases. For the PCLS(0//90) specimen, the FPZ length variations at the initial and migrated interfaces are closely aligned. In contrast, for the PCLS(0//0) specimen, the initial and migrated interfaces exhibit different displacement levels for stable growth due to the distinct cohesive behaviours assigned to each interface. Despite these differences, the virtual FPZ length during stable delamination growth remains comparable between 1D and 2D cases, with the 2D simulations exhibiting a slightly shorter FPZ than the 1D results.

The ERR distribution at the delamination front is also extracted to analyse the influence of misalignment between the fibre orientation and the growth direction on delamination propagation. As shown in Fig. 18, the ERR along the delamination front of the ELS specimens at the corresponding onset displacement level equals $G_{mmc} = J^{init}$. For the 0°//45° interface, the ERR is not uniformly distributed along the delamination front but varies due to the asymmetrical stress state caused by bending/twisting coupling in the 45° ply. This leads to a tilted delamination front that follows the 45° ply orientation (Fig. 10). For stable delamination growth, the ERR along the delamination front is nearly uniform and approximately equal to the total ERR, G^{tot}.

The ERR distributions along the 2D delamination front are extracted and presented in Fig. 18(d)~(f). For the initial delamination front (contour 1), a higher ERR is observed at locations where the normal direction of the front is parallel to the fibre direction, aligned with the maximum principal stress vector. This leads to localised delamination onset at two critical locations (normalised length = 0 or 1). Once damage initiates at these critical points, the stress concentration redistributes along the front, causing a rapid increase in ERR in the surrounding regions. As delamination progresses, the ERR values along the newly formed delamination front stabilise and reach J_{prop}, indicating stable delamination growth.

4.4. Damage evolution in 1D and 2D growth by AE

Since mode II delamination growth is driven by the development and coalescence of shear-induced matrix cracks ahead of the delamination tip [52,62], clustering analysis was performed to distinguish AE events that potentially represent different damage modes at various stages of damage evolution.

The peak frequency of AE events was identified as the most representative feature and was used to classify the AE clusters [63]. As shown in Fig. 19, four distinct clusters with different peak frequency ranges were identified. A statistical analysis was performed, showing that each pair of clusters exhibited significant differences with p-values smaller than 0.05. This indicates that the clusters are clearly distinguishable based on frequency. For the MD specimens, the peak frequencies of the first three clusters exhibit strong similarities, in

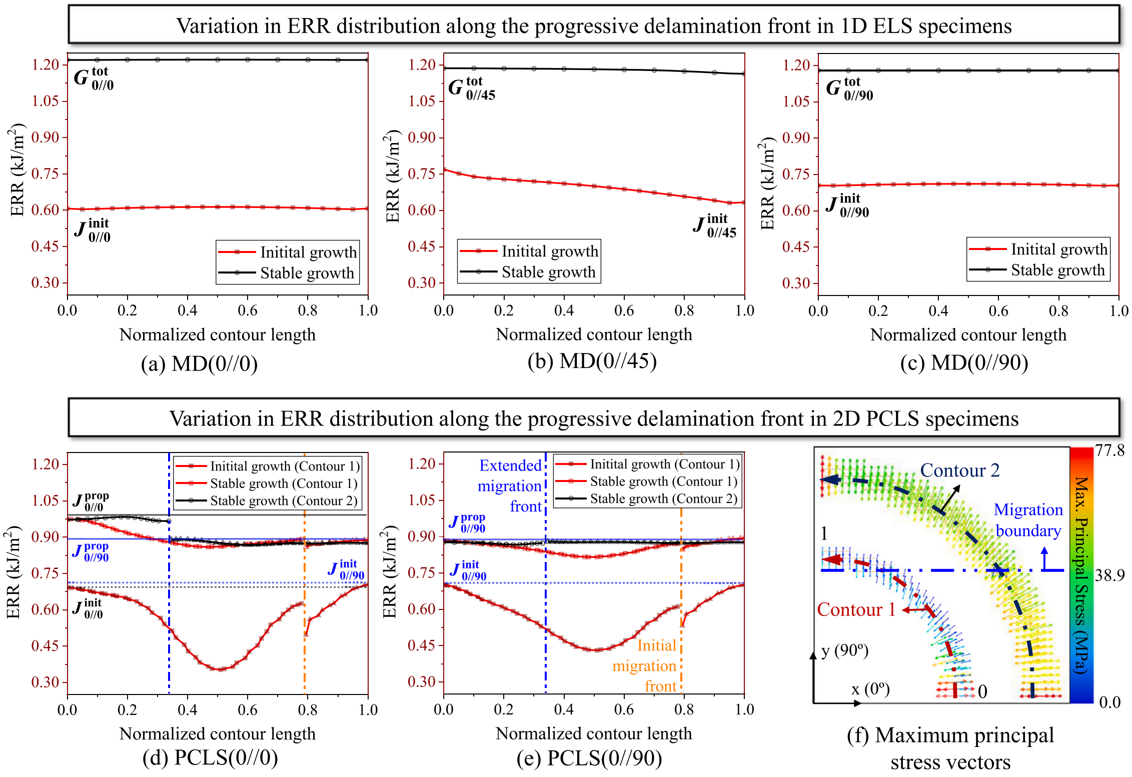

Fig. 18. ERR distribution along the progressive delamination front. For 2D growth, the ERR distribution along the initial delamination front (contour 1) and the propagated delamination front (contour 2) is extracted, as illustrated in (f). For both 1D and 2D growth, the ERR along the delamination front remains nearly constant during the stable growth phase (black curves), but shows variation at the angled interface in the MD(0//45) specimen and in PCLS specimens at delamination onset (red curves). (For interpretation of the references to colour in this figure legend, the reader is referred to the web version of this article.)

contrast to the UD specimen, where more distinct frequency variations are observed.

In 1D tests, the first cluster (orange curves) exhibits the lowest peak frequency, with no distinct onset points identified across the specimens. For the MD(0//45) and MD(0//90) specimens, the second and third clusters display similar peak frequency ranges and onset displacement levels on average. In contrast, for the UD and MD(0//0) specimens, the third cluster shows a significantly higher peak frequency than the second cluster. Moreover, the onset displacement of the third cluster spans a broader range and appears earlier than the second cluster. This variation between the 0°//0° and angled (0°//45° and 0°//90°) interfaces can be attributed to the different bridging effects.

For the 0°//0° interface, extensive fibre bridging is already present near the initial insert after pre-cracking, especially in UD specimen. This promotes earlier fibre–matrix debonding and fibre breakage, which may correspond to the third and fourth AE clusters, respectively. In contrast, for the angled interfaces with less intensive fibre bridging, the third cluster can be associated with delamination growth driven by large-area matrix cracking, while the second cluster corresponds to small-scale matrix cracking.

To determine the onset point for each cluster, Sentry function curves were analysed [64]. A drop in the curve signifies increased AE energy or load drop, indicating damage onset [65]. The onset points (displacement levels) correspond to the local extreme in the Sentry function curves, marked by vertical dashed lines in Fig. 19. The drop in the Sentry function near the force decrease can be correlated to the onset of delamination growth [45,65].

Compared to 1D results, the onset points are less consistent in 2D tests. The first few drops in the Sentry function curve can be considered as potential onset points. A statistical analysis was performed to determine the onset deflection levels and peak frequencies of different clusters. The results are summarised in Fig. 20.

The 1st cluster, characterised by the lowest peak frequency, exhibits a significant difference between the 1D and 2D tests. This discrepancy is likely associated with friction-generated AE signals, which vary notably under the distinct test conditions. For PCLS specimens, the 2nd and 3rd clusters show similar peak frequency ranges to those observed in the 1D tests. The mean onset deflection of the 2nd cluster is lower than that of the 3rd cluster, indicating that the 2nd cluster can be correlated with the matrix cracking event. The 3rd cluster, with higher onset deflection levels and peak frequency ranges, can be attributed to a combination of matrix crack coalescence and fibre–matrix debonding in the PCLS(0//0) specimen. For the PCLS(0//90) specimen, it aligns with delamination growth involving large-area matrix cracking. The 4th cluster, characterised by the highest peak frequency and onset displacement level, may be associated with fibre pullout and fibre breakage, which result from bridging zone development in 1D tests and flexural failure in 2D tests. The clustering results also show strong agreement with the peak frequency ranges reported in Ref. [66] for 1D tests and Ref. [67] for 2D tests.

The corresponding displacement (1D) or deflection (2D) levels of various delamination phases predicted using the modified cohesive model from Fig. 17 are summarised in Fig. 20, along with the AE clustering results. The displacement levels for initial and stable delamination growth fall within the range of the 2nd and 3rd AE clusters, which correspond to matrix cracking and fibre–matrix debonding (or delamination) events. Total failure aligns with fibre breakage events identified in the 4th cluster for 1D tests. While the AE clusters capture the actual damage events observed in physical tests, the numerical model offers an idealised prediction of the onset of different damage phases in the mode II delamination process.

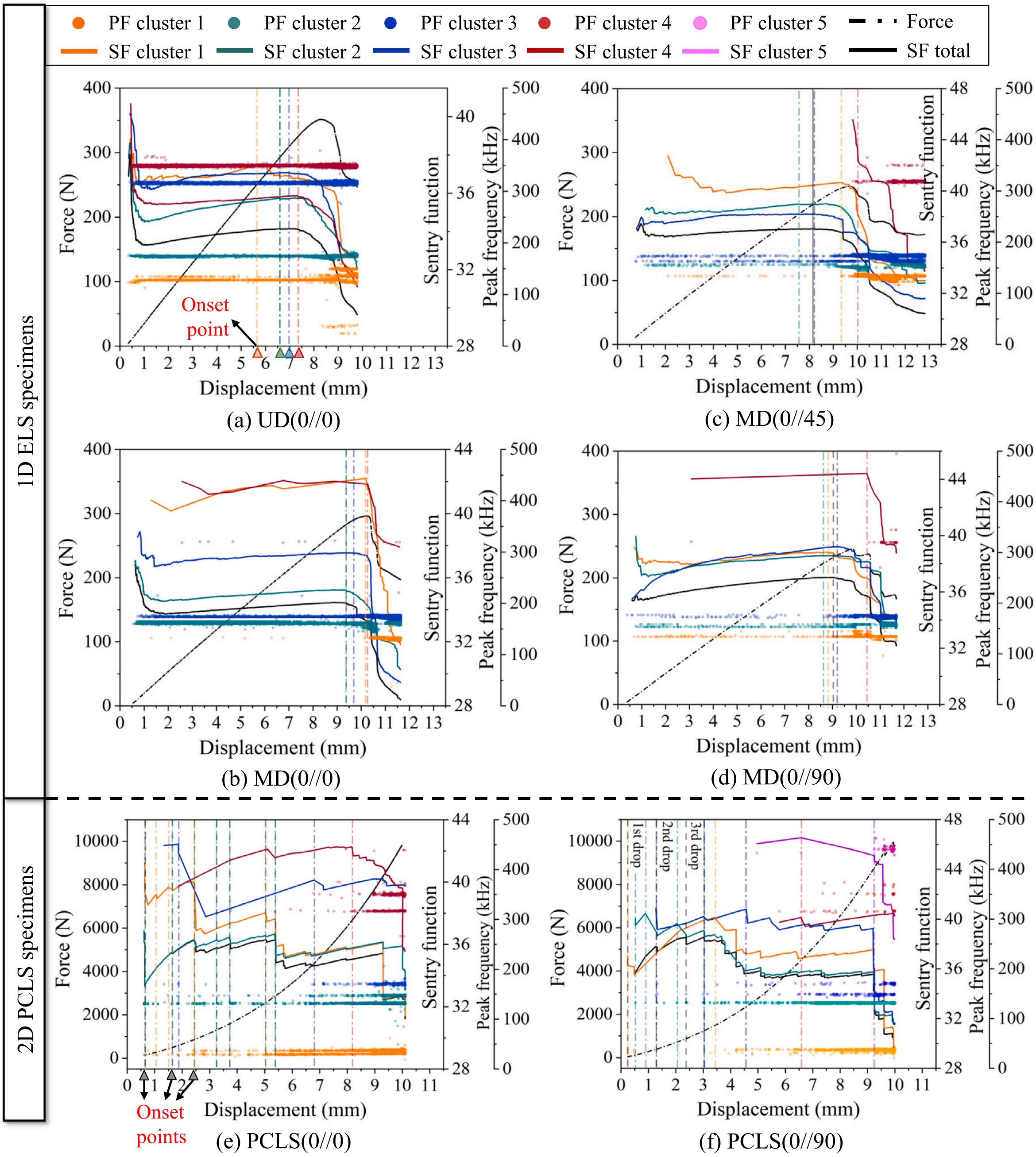

(a) UD(0//0)

(c) MD(0//45)

(b) MD(0//0)

(d) MD(0//90)

(e) PCLS(0//0)

(f) PCLS(0//90)

Fig. 19. Example of AE clustering results for 1D and 2D experiments of a single specimen. The full dataset is publicly available and can be accessed via the link provided in the Data Availability section. The sentry function (SF) curves for all AE events and individual clusters are depicted as solid lines. The peak frequencies (PF) of AE events assigned to different clusters are also provided. For ELS specimens, the onset point of each AE cluster is identified by the initial drop in the SF curves. For PCLS specimens, the onset is less distinct and is therefore defined as a displacement range within the first few drops in the SF curves.

5. Discussion

5.1. The effect of misalignment between fibre orientation and growth direction

For quasi-static delamination growth in 1D, distinct delamination mechanisms can be identified at different interfaces, as demonstrated by SEM observations (Fig. 21) and AE clustering (Fig. 20). However, the intrinsic fracture toughness, $G_{IIc}^{intrinsic} = J^{prop}$, is not significantly influenced by the interface angle, as illustrated in Fig. 9. Although the fracture morphologies vary across different interfaces, the propagation follows the 0° ply, where shear-induced matrix cracks cannot propagate further into the 0° layer. In this case, only interlaminar matrix cracking — specifically, the formation of cusps — contributes to the intrinsic fracture resistance.

As shown in the third column of Fig. 21, the presence of small cusps within the large matrix cracking region indicates that the delamination growth direction follows the maximum principal stress (Fig. 18-f). For ELS tests, such matrix cracking patterns do not significantly influence the intrinsic fracture toughness. However, in 2D delamination growth, less propagation is observed in the diagonal direction, where there is a misalignment angle θ between the fibre orientation and the growth direction. Delamination growth in this direction is equivalent to propagation at a $-\theta°// + \theta°$ interface, where matrix cracks may propagate further into the $\theta°$ ply, driven by mixed-mode II/III loading.

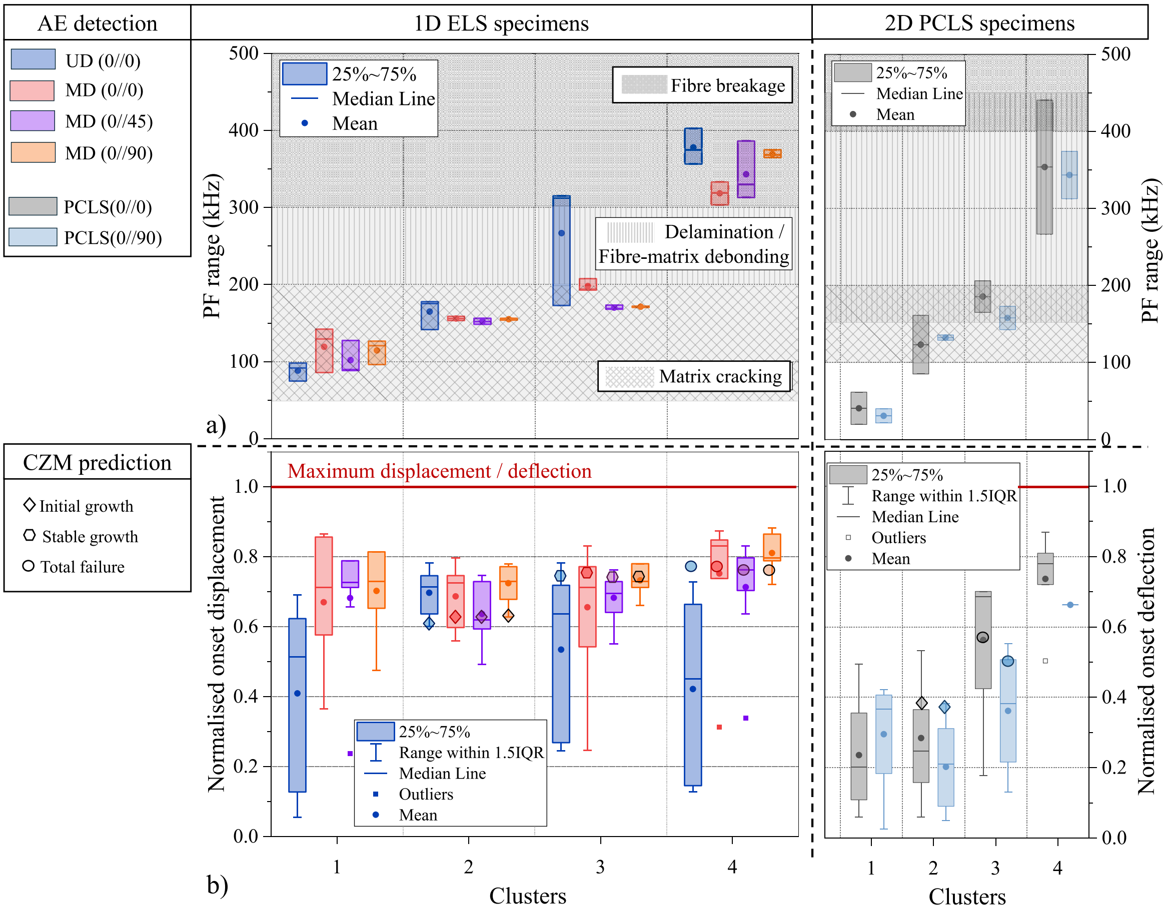

Fig. 20. (a) Statistical analysis of AE clustering results from 1D and 2D experiments. The peak frequency (PF) ranges for different damage events in a different CFRP material system (Ref.[66]) and the same material system (Ref.[67]) are shown in the upper left and right figures, respectively, using distinct pattern regions. These PF ranges are comparable to those of the AE clusters identified in the present study, represented by floating bars. (b) Statistical analysis of onset displacement levels for each cluster across different specimen configurations, alongside numerical predictions for delamination onset, stable growth, and total failure, each indicated by distinct marker shapes. '1.5IQR' denotes the 1.5 times Interquartile Range, representing the upper and lower bounds of data dispersion, '25%' indicates the first quartile, while '75%' indicates the third quartile.

Consequently, the formation of a larger delamination area involves additional intralaminar damage mechanisms, resulting in higher fracture resistance.

The characterisation of mode II 2D delamination growth can primarily focus on regions where delamination propagates along the fibre direction. However, as the contribution of mode III increases with further delamination propagation, delamination may migrate again and continue to propagate at a more critical interface, depending on the stacking sequence. Accurate prediction of the migration phenomenon is, therefore, essential for reliably predicting planar delamination growth.

5.2. In-plane stretching effect

For the 1D ELS model, the shape of the cohesive constitutive model has no significant influence on the delamination behaviour or the force–displacement response, provided the total fracture toughness G_{IIc}^{tot} remains constant. However, this is not the case for 2D delamination growth. As shown in Fig. 16, the bilinear cohesive model, when using only the intrinsic fracture toughness, overestimates delamination growth at the initial interface (blue dotted line). By modifying the shape of the cohesive model using a UMAT (red solid line), a larger critical separation for the final failure, δ_3 in Eq. (12), results in a smaller predicted delamination growth, even when the same intrinsic fracture toughness is applied (Fig. 7). This indicates that predicting 2D delamination growth using CZM is highly sensitive to the shape of the cohesive law, particularly the critical displacement jump. This sensitivity arises from additional in-plane stretching in the 2D PCLS test, which modifies the local stress state and strain distribution.

In-plane stretching plays a pivotal role in planar delamination tests [16,68]. The radial membrane stress in tension acts as an additional opening force, facilitating delamination growth [68,69]. As shown in Fig. 22, the opening stress σ_{11} in the PCLS specimen promotes matrix cracking, resulting in less sharp cusps and larger gaps between them. The difference in the local stress state between 1D and 2D delamination fronts significantly influences the formation of cusps. The contribution of σ_{11} to mode II delamination growth would not exist if delamination is modelled as a flat plane without thickness, as is commonly assumed.

Since the stress state at the delamination front influences cohesive behaviour, the calibrated cohesive parameters cannot be directly applied to predict 2D delamination growth. Additionally, extrinsic toughening mechanisms are strongly influenced by interface properties. The higher total fracture toughness G_{IIc}^{tot} observed in the UD specimen is primarily due to large-scale fibre bridging at the 0°//0° interface, which is facilitated by fibre nesting. However, such large-scale bridging effects were not observed in 2D delamination growth with a 0°//0° interface. Therefore, the intrinsic fracture toughness should be employed for predicting delamination growth without bridging effects, although it provides a conservative prediction by overestimating delamination growth. The same applies to the 0°//90° interface, with less bridging effects.

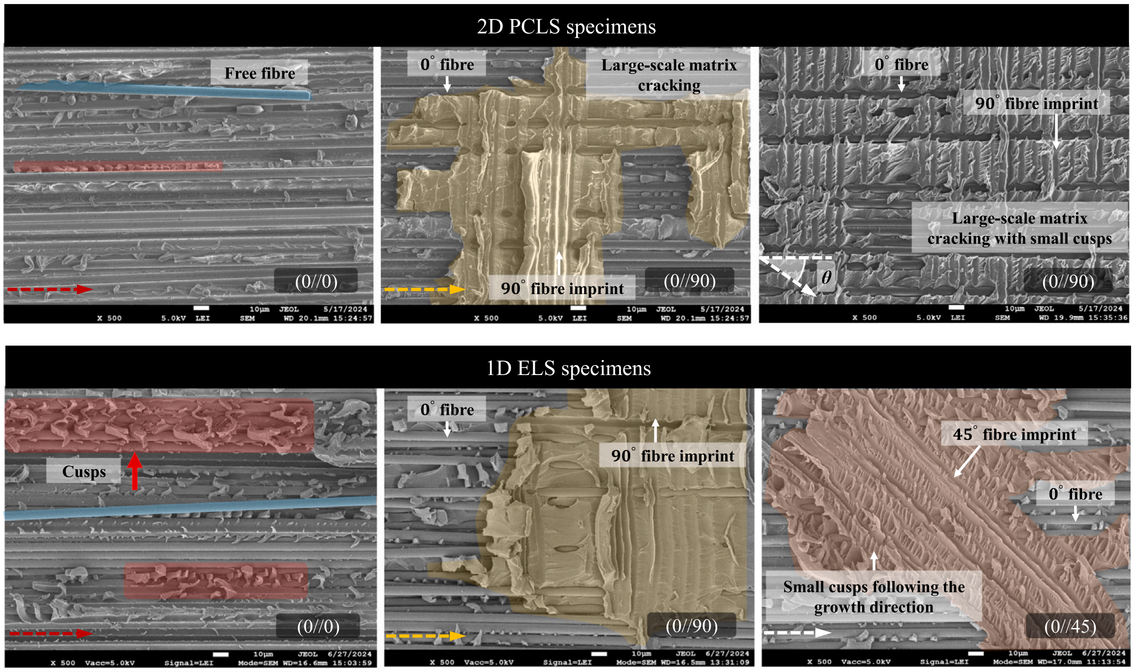

Fig. 21. Comparison in the fracture surface morphologies between 1D ELS and 2D PCLS specimens. The interface angles are indicated in the bottom-right corner, while the arrows in the bottom-left corner denote the delamination growth direction.

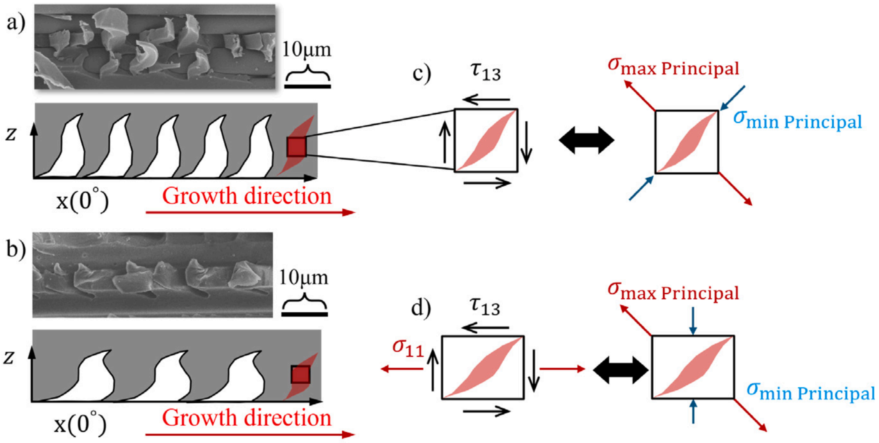

Fig. 22. Illustration of the progressive delamination growth and local stress state for ELS UD(0//0) specimen, (a) and (c), PCLS(0//0) specimen, (b) and (d).

Using the bilinear model with either intrinsic or total fracture toughness and $\tau^0 = Y_T$ provides a prediction band for 2D delamination growth following the fibre direction. Tuning the shape of the cohesive model can achieve better agreement with experimental results; however, this is highly dependent on the experimental setup, local stress state, and active delamination mechanisms. The stretching effect, which is induced by boundary constraints, can also be affected by the specimen geometry [68]. Further investigation into these contributing factors is necessary to support the development of generalised numerical or analytical tools for predicting planar delamination growth.

6. Conclusions

This work presents a comprehensive comparison of 1D and 2D mode II delamination growth, both experimentally and numerically. To gain a better understanding of the delamination process, various experimental monitoring techniques were employed to track delamination growth in CFRP laminates. The decomposed fracture toughness, derived from standard 1D tests, was used in the modified cohesive model to simulate both 1D and 2D growth. Various cohesive constitutive models were determined by numerically tuning the parameters to align with the experimental results.

The intrinsic fracture toughness can be influenced by the specimen stiffness due to its effect on the geometric nonlinearity in the J-integral calculation. The interface angle exhibits negligible influence on the intrinsic fracture toughness, despite the distinct fracture surface morphologies observed at different interfaces. On the other hand, extrinsic toughening is affected by both the interface properties and the specimen stiffness.

Although similar damage modes and damage processes are identified in 1D and 2D tests, the extrinsic toughening mechanisms are distinct between 1D and 2D mode II growth. Using fracture toughness with or without the extrinsic toughening components in the bilinear cohesive model can lead to either underestimation or overestimation of 2D delamination growth.

Compared to the bilinear cohesive law, the modified cohesive model provides better predictions of the force–displacement responses and delamination evolution for the 1D case. However, it cannot be directly applied to the 2D model, as identical extrinsic toughening mechanisms, such as large-scale fibre bridging, may not be present. For 2D growth, excluding the extrinsic toughening in the numerical simulation can yield better alignment with experimental results. This can be achieved by introducing additional control parameters that offer a more accurate description of the interface fracture behaviour.

The modified cohesive model offers flexibility in adjusting the controlling parameters to accurately capture mode II delamination behaviour. However, the calibration of these parameters relies on manual tuning, which may vary depending on changes in experimental conditions or specimen configurations. Accurate prediction of the delamination process using CZM requires proper identification of the governing damage and toughening mechanisms. The use of 1D data from UD specimens to predict 2D delamination growth across various interfaces must be carefully validated, as the extrinsic toughening mechanisms can vary significantly between 1D and 2D scenarios. The intrinsic fracture toughness is suggested for a conservative design in engineering applications.

CRediT authorship contribution statement

Wenjie Tu: Writing – review & editing, Writing – original draft, Methodology, Investigation, Formal analysis, Data curation, Conceptualization. **John-Alan Pascoe:** Writing – review & editing, Supervision, Resources, Methodology, Conceptualization. **René Alderliesten:** Writing – review & editing, Supervision, Resources, Methodology, Conceptualization.

Declaration of competing interest

The authors declare that they have no known competing financial interests or personal relationships that could have appeared to influence the work reported in this paper.

Acknowledgements

The authors gratefully acknowledge the financial support from the China Scholarship Council (No. CSC202006950073).

Appendix 7

7.1. Cohesive constitutive law

The cohesive constitutive law is defined as [70]:

$$\tau = \left\{ \begin{array}{c} \tau_1 \\ \tau_2 \\ \tau_3 \end{array} \right\} = (1-d)K \left\{ \begin{array}{c} \delta_1 \\ \delta_2 \\ \delta_3 \end{array} \right\} \tag{1}$$

where $\tau_i (i = 1,2,3)$ are the traction components, $\delta_i (i = 1,2,3)$ are the displacement jump in three directions, d is the damage variable, and K is the undamaged penalty stiffness.

The norm of the displacement tensor is defined as:

$$\lambda = \sqrt{< \delta_3 >^2 + (\delta_1)^2 + (\delta_2)^2} \tag{2}$$

where δ_3 is the normal displacement jump, $< \cdot >$ is the Macaulay bracket defined as $< x > = \frac{1}{2}(x+|x|)$, which omits negative displacement jump in compression. δ_1 and δ_2 are the shear displacement jump in mode II and mode III, respectively. It should be noted that mixed-mode effects on stiffness, discussed in Ref. [27], are not considered here, since delamination growth is predominantly driven by mode II.

7.2. Damage onset

The onset of cohesive failure is defined by Ye's criterion [71], using a quadratic interaction of the traction tensor:

$$\left(\frac{< \tau_3 >}{\tau_3^0} \right)^2 + \left(\frac{\tau_1}{\tau_1^0} \right)^2 + \left(\frac{\tau_2}{\tau_2^0} \right)^2 = 1 \tag{3}$$

where $\tau_i^0 (i = 1,2,3)$ indicates the critical interface strength in three directions.

The criterion can be also implemented in the displacement jump space:

$$\left(\frac{< \delta_3 >}{\delta_3^0} \right)^2 + \left(\frac{\delta_1}{\delta_1^0} \right)^2 + \left(\frac{\delta_2}{\delta_2^0} \right)^2 = 1 \tag{4}$$

where the critical displacement tensor $\delta_i^0 (i = 1,2,3)$ can be calculated using $\delta_i = \frac{\tau_i}{K}$, with the assumption that the penalty stiffness is the same for normal and shear tractions.

The cohesive damage variable is updated when the following criterion is satisfied:

$$F(\lambda^t, r^t) := \lambda^t - r^t \le 0, \forall t \ge 0 \tag{5}$$

where t indicates the actual time and r^t is the displacement jump at the current damage states d_t. Damage evolves when the norm of the displacement tensor λ exceeds the threshold displacement jump r^t, and Eq. (5) returns *False*. r^0 equals δ^0 for damage onset.

7.3. Damage evolution law

The traditional bilinear damage evolution law is defined as follows:

$$d(\lambda) = \frac{\delta^f (\lambda - \delta^0)}{\lambda (\delta^f - \delta^0)} \tag{6}$$

where the δ^0 is the onset displacement threshold, δ^f is the failure displacement jump.

The area under the traction-separation law is equal to the fracture toughness:

$$G_{ic} = \frac{1}{2} K \delta^0 \delta^f \tag{7}$$

where $G_{ic} (i = I, II, III)$ are the fracture toughness for pure mode I, mode II, and mode III fracture.

7.4. Modified damage evolution law

A multi-point damage evolution law is developed based on the decomposition of G_{IIc} into intrinsic resistance and extrinsic toughening as follows:

$$G_{IIc} = G_{IIc}^{intrinsic} + G_{IIc}^{extrinsic} \tag{8}$$

where the intrinsic resistance $G_{IIc}^{intrinsic}$ and $G_{IIc}^{extrinsic}$ can be further decomposed as:

$$G_{IIc}^{intrinsic} = G_{mmc} + G_{delam} \tag{9}$$

where G_{mmc} is the ERR for micro matrix cracking determined by J^{init}, G_{delam} is the ERR for the coalescence of matrix cracks that forms delamination calculated by $J^{prop} - J^{init}$, G_{eff} is the extrinsic toughening calculated by $G_{IIc}^{tot} - J^{prop}$. G_{eff} is further decomposed into effective toughening G_{eff}^T due to fibre bridging and interface friction, and G_{eff}^{fb} from fibre breakage. γ is a numerical coefficient that needs to be defined to determine the proportion of the extrinsic ERR caused effective toughening and fibre breakage:

$$G_{IIc}^{extrinsic} = G_{eff}^T + G_{eff}^{fb} = \gamma G_{eff} + (1-\gamma) G_{eff} \tag{10}$$

Four traction parameters $\tau^i (i = 0,1,2,3)$ are defined in the damage evolution law. It is worth mention that mode dependency is not included in the modified cohesive law. Therefore, the corresponding displacement jump thresholds $\delta^i (i = 0, 1, 2, 3, f)$ can be calculated based on the decomposed ERR components:

$$\begin{cases} \delta^0 = \dfrac{\tau}{K} \\ \delta^1 = \dfrac{2G_{mmc} + \delta^0 \tau 1}{\tau^0} \\ \delta^2 = \dfrac{2G_{delam}}{\tau^1 + \tau^2} + \delta^1 \\ \delta^3 = \dfrac{2G_{eff}^{T}}{\tau^2 + \tau^3} + \delta^2 \\ \delta^f = \dfrac{2G_{eff}^{fb}}{\tau^3} + \delta^3 \end{cases} \tag{11}$$

The corresponding damage variable can be calculated as a function of λ using the cohesive parameters:

$$d(\lambda) = \begin{cases} 0 & , \lambda \le \delta^0 \\ \dfrac{K\delta^1(\lambda - \delta^0) + \tau^1(\delta^0 - \lambda)}{K\lambda(\delta^1 - \delta^0)} & , \delta^0 < \lambda \le \delta^1 \\ 1 + \dfrac{\lambda(\tau^1 - \tau^2) + \delta^1\tau^2 - \delta^2\tau^1}{K\lambda(\delta^2 - \delta^1)} & , \delta^1 < \lambda \le \delta^2 \\ 1 + \dfrac{\lambda(\tau^2 - \tau^3) + \delta^2\tau^3 - \delta^3\tau^2}{K\lambda(\delta^3 - \delta^2)} & , \delta^2 < \lambda \le \delta^3 \\ 1 + \dfrac{\tau^3(\lambda - \delta^f)}{K\lambda(\delta^f - \delta^3)} & , \lambda > \delta^3 \end{cases} \tag{12}$$

Data availability

The experimental dataset is available for download from: https://doi.org/10.4121/ec008223-1408-481db641-d6e7903dd594.

References

[1] Santos M, Santos J, Reis P, Amaro A. Ultrasonic C-scan techniques for the evaluation of impact damage in CFRP. Mater Test 2021;63(2):131–7. http://dx.doi.org/10.1515/mt-2020-0020.

[2] Morokov E, Levin V, Chernov A, Shanygin A. High resolution ply-by-ply ultrasound imaging of impact damage in thick CFRP laminates by high-frequency acoustic microscopy. Compos Struct 2021;256:113102. http://dx.doi.org/10.1016/j.compstruct.2020.113102, URL https://www.sciencedirect.com/science/article/pii/S0263822320330282.

[3] Ellison A, Kim H. Shadowed delamination area estimation in ultrasonic C-scans of impacted composites validated by X-ray CT. J Compos Mater 2020;54(4):549–61. http://dx.doi.org/10.1177/0021998319865311.

[4] Kimura M, Watanabe T, Oshima S, Takeichi Y, Niwa Y, Seryo Y, Hojo M. Nanoscale in situ observation of damage formation in carbon fiber/epoxy composites under mixed-mode loading using synchrotron radiation X-ray computed tomography. Compos Sci Technol 2022;230:109332. http://dx.doi.org/10.1016/j.compscitech.2022.109332, URL https://www.sciencedirect.com/science/article/pii/S0266353822000744.

[5] Biagini D, Pascoe J-A, Alderliesten R. Investigating apparent plateau phases in fatigue after impact damage growth in CFRP with ultrasound scan and acoustic emissions. Int J Fatigue 2023;177:107957. http://dx.doi.org/10.1016/j.ijfatigue.2023.107957, URL https://www.sciencedirect.com/science/article/pii/S0142112323004589.

[6] ASTM D5528-01. Standard test method for mode I interlaminar fracture toughness of unidirectional fiber-reinforced polymer matrix composites. Am Stand Test Methods 2014;03(Reapproved 2007). http://dx.doi.org/10.1520/D5528-13.2.

[7] ASTM D7905. Standard test method for determination of the mode II interlaminar fracture toughness of unidirectional fiber-reinforced polymer matrix composites. ASTM 2014. http://dx.doi.org/10.1520/D7905.

[8] McElroy MW, Gutkin R, Pankow M. Interaction of delaminations and matrix cracks in a CFRP plate, Part II: Simulation using an enriched shell finite element model. Compos Part A: Appl Sci Manuf 2017;103:252–62. http://dx.doi.org/10.1016/j.compositesa.2017.10.006.

[9] Hu P, Pulungan D, Tao R, Lubineau G. An experimental study on the influence of intralaminar damage on interlaminar delamination properties of laminated composites. Compos Part A: Appl Sci Manuf 2020;131(January):105783. http://dx.doi.org/10.1016/j.compositesa.2020.105783.

[10] Pichler N, Herráez M, Botsis J. Mixed-mode fracture response of anti-symmetric laminates: Experiments and modelling. Compos Part B: Eng 2020;197:108089. http://dx.doi.org/10.1016/j.compositesb.2020.108089, URL https://www.sciencedirect.com/science/article/pii/S1359836820313639.

[11] Ramji A, Xu Y, Yasaee M, Grasso M, Webb P. Delamination migration in CFRP laminates under mode I loading. Compos Sci Technol 2020;190:108067. http://dx.doi.org/10.1016/j.compscitech.2020.108067, URL https://www.sciencedirect.com/science/article/pii/S0266353819317919.

[12] Herráez M, Pichler N, Pappas GA, Blondeau C, Botsis J. Experiments and numerical modelling on angle-ply laminates under remote mode II loading. Compos Part A: Appl Sci Manuf 2020;134(March):105886. http://dx.doi.org/10.1016/j.compositesa.2020.105886.

[13] Hu P. New tools for the description of intra / inter laminar coupling in laminates : experimental evidence and modeling approaches ping [Ph.D. thesis], King Abdullah University of Science and Technology; 2022.

[14] Gong Y, Zhao L, Zhang J, Wang Y, Hu N. Delamination propagation criterion including the effect of fiber bridging for mixed-mode I/II delamination in CFRP multidirectional laminates. Compos Sci Technol 2017;151:302–9. http://dx.doi.org/10.1016/j.compscitech.2017.09.002.

[15] Shi C, Xu W. Effects of friction and strain hardening on ELS mode II interlaminar fracture test. Compos Struct 2023;313:116942. http://dx.doi.org/10.1016/j.compstruct.2023.116942, URL https://www.sciencedirect.com/science/article/pii/S0263822323002866.

[16] Cameselle-Molares A, Vassilopoulos AP, Renart J, Turon A, Keller T. Numerical simulation of two-dimensional in-plane crack propagation in FRP laminates. Compos Struct 2018;200:396–407. http://dx.doi.org/10.1016/j.compstruct.2018.05.136.

[17] Hu P, Tao R, Li X, Lubineau G. Decomposing the coupling damage in mode I multidirectional delamination. Compos Sci Technol 2022;229:109684. http://dx.doi.org/10.1016/j.compscitech.2022.109684, URL https://www.sciencedirect.com/science/article/pii/S0266353822004262.

[18] Wang C, Vassilopoulos AP, Keller T. Numerical investigation of two-dimensional Mode-II delamination in composite laminates. Compos Part A: Appl Sci Manuf 2024;179(January):108012. http://dx.doi.org/10.1016/j.compositesa.2024.108012.

[19] Canturri C, Greenhalgh ES, Pinho ST. The relationship between mixed-mode II/III delamination and delamination migration in composite laminates. Compos Sci Technol 2014;105:102–9. http://dx.doi.org/10.1016/j.compscitech.2014.10.001, URL https://www.sciencedirect.com/science/article/pii/S0266353814003558.

[20] Tu W, Pascoe J-A, Alderliesten R. Planar delamination behaviour of CFRP panels under quasi-static out-of-plane loading. Compos Struct 2024;339:118137. http://dx.doi.org/10.1016/j.compstruct.2024.118137, URL https://www.sciencedirect.com/science/article/pii/S0263822324002654.

[21] Ye Q, Chen P. Prediction of the cohesive strength for numerically simulating composite delamination via CZM-based FEM. Compos Part B: Eng 2011;42(5):1076–83. http://dx.doi.org/10.1016/j.compositesb.2011.03.021.

[22] Hongkarnjanakul N, Bouvet C, Rivallant S. Validation of low velocity impact modelling on different stacking sequences of CFRP laminates and influence of fibre failure. Compos Struct 2013;106:549–59. http://dx.doi.org/10.1016/j.compstruct.2013.07.008, URL https://www.sciencedirect.com/science/article/pii/S0263822313003309.

[23] Pigazzini MS, Bazilevs Y, Ellison A, Kim H. A new multi-layer approach for progressive damage simulation in composite laminates based on isogeometric analysis and Kirchhoff–Love shells. Part II: impact modeling. Comput Mech 2018;62(3):587–601. http://dx.doi.org/10.1007/s00466-017-1514-0.

[24] Baluch AH, Falcó O, Jiménez JL, Tijs BH, Lopes CS. An efficient numerical approach to the prediction of laminate tolerance to Barely Visible Impact Damage. Compos Struct 2019;225:111017. http://dx.doi.org/10.1016/j.compstruct.2019.111017, URL https://www.sciencedirect.com/science/article/pii/S0263822319301199.

[25] Batmaz OA, Bozkurt MO, Gurses E, Coker D. High-fidelity simulations of low-velocity impact induced matrix cracking and dynamic delamination progression in CFRP beams. Compos Part A: Appl Sci Manuf 2024;177:107960. http://dx.doi.org/10.1016/j.compositesa.2023.107960, URL https://www.sciencedirect.com/science/article/pii/S1359835X23005365.

[26] Chen BY, Pinho ST, De Carvalho NV, Baiz PM, Tay TE. A floating node method for the modelling of discontinuities in composites. Eng Fract Mech 2014;127:104–34. http://dx.doi.org/10.1016/j.engfracmech.2014.05.018.

[27] Turon A, González EV, Sarrado C, Guillamet G, Maimí P. Accurate simulation of delamination under mixed-mode loading using a cohesive model with a mode-dependent penalty stiffness. Compos Struct 2018;184(June 2017):506–11. http://dx.doi.org/10.1016/j.compstruct.2017.10.017.

[28] Grosselle R, Lindgaard E, Olesen AM, Jensen SM, Bak BLV. Simulation of fibre bridging in mixed mode I–II delamination of unidirectional composite laminates via discrete modelling of fibre bundles. Compos Part A: Appl Sci Manuf 2025;199(000). http://dx.doi.org/10.1016/j.compositesa.2025.109247.

[29] Ai X, Chen B, Kassapoglou C. Structural cohesive element for the modelling of delamination in composite laminates without the cohesive zone limit. Eng Fract Mech 2025;329(000). http://dx.doi.org/10.1016/j.engfracmech.2025.111586.

[30] Dang W, Wang J, Ni A. Simulation of unidirectional composite delamination using fiber bundle interface strength. Theor Appl Fract Mech 2025;138(000). http://dx.doi.org/10.1016/j.tafmec.2025.104915.

[31] Shirzadeh Z, Fakoor M, Daneshjoo Z. Simulating delamination in composite laminates with fracture process zone effects: A novel cohesive zone modeling approach. Eng Fract Mech 2025;315. http://dx.doi.org/10.1016/j.engfracmech.2025.110834.

[32] Wolf CH, Düreth C, Wünsche M, Henkel S, Tittmann K, Gude M, Biermann H. Fatigue delamination growth in textile-reinforced plastics under combined interlaminar shear and compression: Numerical and experimental characterization. Compos Struct 2025;371(000). http://dx.doi.org/10.1016/j.compstruct.2025.119384.

[33] Taghavian SH, Ghasemi AR. A unified approach to the effect of in-plane biaxial loading on delamination progression in laminated composite structures. Compos Sci Technol 2025;267(000). http://dx.doi.org/10.1016/j.compscitech.2025.111185.

[34] Delta-tech. Matrix technical data sheet - DT120 versatile high toughness epoxy matrix. Tech. rep. Delta-tech; 2015.

[35] Bin Mohamed Rehan M, Rousseau J, Fontaine S, Gong X. Experimental study of the influence of ply orientation on DCB mode-I delamination behavior by using multidirectional fully isotropic carbon/epoxy laminates. Compos Struct 2017;161:1–7. http://dx.doi.org/10.1016/j.compstruct.2016.11.036, URL https://www.sciencedirect.com/science/article/pii/S0263822316307061.

[36] Völkerink O, Koord J, Petersen E, Hühne C. Holistic determination of physical fracture toughness values and numerical parameters for delamination analysis considering multidirectional-interfaces. Compos Part C: Open Access 2022;8:100277. http://dx.doi.org/10.1016/j.jcomc.2022.100277, URL https://www.sciencedirect.com/science/article/pii/S2666682022000408.

[37] Pérez-Galmés M, Renart J, Sarrado C, Rodríguez-Bellido A, Costa J. A data reduction method based on the J-integral to obtain the interlaminar fracture toughness in a mode II end-loaded split (ELS) test. Compos Part A: Appl Sci Manuf 2016;90:670–7. http://dx.doi.org/10.1016/j.compositesa.2016.08.020, URL https://www.sciencedirect.com/science/article/pii/S1359835X16302767.

[38] Tu W, Pascoe J-A, Alderliesten R. Comparison of mode II delamination behaviours in multidirectional and unidirectional composite laminates. Compos Part B: Eng 2025;291:111941. http://dx.doi.org/10.1016/j.compositesb.2024.111941, URL https://www.sciencedirect.com/science/article/pii/S1359836824007534.

[39] ISO-15114. Determination of the mode II fracture resistance for unidirectionally reinforced materials using the calibrated end-loaded split test and an eefective crack length approach. 2014, International Standard.

[40] Ding Z, Gong Y, Wang Z, Zhang Y, Hu N. A semi-analytical method for the determination of fracture toughness and bridging law in ELS test. Theor Appl Fract Mech 2023;123:103712. http://dx.doi.org/10.1016/j.tafmec.2022.103712, URL https://www.sciencedirect.com/science/article/pii/S016784422200461X.

[41] Baccar D, Söffker D. Identification and classification of failure modes in laminated composites by using a multivariate statistical analysis of wavelet coefficients. Mech Syst Signal Process 2017;96:77–87. http://dx.doi.org/10.1016/j.ymssp.2017.03.047, URL https://www.sciencedirect.com/science/article/pii/S0888327017301826.

[42] Zhou W, zheng Zhao W, nan Zhang Y, jun Ding Z. Cluster analysis of acoustic emission signals and deformation measurement for delaminated glass fiber epoxy composites. Compos Struct 2018;195:349–58. http://dx.doi.org/10.1016/j.compstruct.2018.04.081, URL https://www.sciencedirect.com/science/article/pii/S026382231733489X.

[43] Lima RA, Tao R, Bernasconi A, Carboni M, Teixeira de Freitas S. Acoustic emission approach for identifying fracture mechanisms in composite bonded Joints: A study on varying Substrate's stacking sequence. Theor Appl Fract Mech 2024;132(February):104490. http://dx.doi.org/10.1016/j.tafmec.2024.104490.

[44] Zhang F, Yang Y, Fennis SA, Hendriks MA. Developing a new acoustic emission source classification criterion for concrete structures based on signal parameters. Constr Build Mater 2022;318:126163. http://dx.doi.org/10.1016/j.conbuildmat.2021.126163.

[45] Saeedifar M, Najafabadi MA, Zarouchas D, Toudeshky HH, Jalalvand M. Clustering of interlaminar and intralaminar damages in laminated composites under indentation loading using Acoustic Emission. Compos Part B: Eng 2018;144:206–19. http://dx.doi.org/10.1016/j.compositesb.2018.02.028, URL https://www.sciencedirect.com/science/article/pii/S1359836817343718.

[46] Lu H, Zheng T, Zhang L, Huang K, Liu X, Han X, Wang Y, Guo L. Damage identification of plain-woven composites at T > Tg using AE: Damage clustering and initiation detection. Compos Sci Technol 2024;257(August):110823. http://dx.doi.org/10.1016/j.compscitech.2024.110823.

[47] Murtagh F. A survey of recent advances in hierarchical clustering algorithms. Comput J 1983;26(4):354–9. http://dx.doi.org/10.1093/comjnl/26.4.354.

[48] Michal S, Szymon D, Pawel Z, Pawel S. Damage characterisation of GFRP composites based on clustering acoustic emission events utilizing single-failure-cause tests as reference. Compos Struct 2025;(Jan.):351. http://dx.doi.org/10.1016/j.compstruct.2024.118596.

[49] Krueger R, Carvalho NVD. A benchmark example for delamination propagation predictions based on the calibrated end-loaded split specimen. Tech. rep. NASA/TM20220002098; 2022.

[50] Shahzad M, Kamran A, Siddiqui MZ, Farhan M. Mechanical characterization and FE modelling of a hyperelastic material. Mater Res 2015;18(5):918–24. http://dx.doi.org/10.1590/1516-1439.320414.

[51] Yeoh OH. Some forms of the strain energy function for rubber. Rubber Chem Technol 1993;66(5):754–71. http://dx.doi.org/10.5254/1.3538343, arXiv:https://meridian.allenpress.com/rct/article-pdf/66/5/754/1942809/1_3538343.pdf.

[52] Amaral L, Alderliesten R, Benedictus R. Towards a physics-based relationship for crack growth under different loading modes. Eng Fract Mech 2018;195:222–41. http://dx.doi.org/10.1016/j.engfracmech.2018.04.017, URL https://www.sciencedirect.com/science/article/pii/S0013794417309001.

[53] Pappas G, Botsis J. Intralaminar fracture of unidirectional carbon/epoxy composite: experimental results and numerical analysis. Int J Solids Struct 2016;85–86:114–24. http://dx.doi.org/10.1016/j.ijsolstr.2016.02.007, URL https://www.sciencedirect.com/science/article/pii/S0020768316000615.

[54] Gong Y, Hou Y, Zhao L, Li W, Zhang J, Hu N. A modified mode I cohesive zone model for the delamination growth in DCB laminates with the effect of fiber bridging. Int J Mech Sci 2020;176(August 2019):105514. http://dx.doi.org/10.1016/j.ijmecsci.2020.105514.

[55] Yao L, Liu J, Lyu Z, Alderliesten R, Hao C, Ren C, Guo L. In-situ damage mechanism investigation and a prediction model for delamination with fibre bridging in composites. Eng Fract Mech 2023;281:109079. http://dx.doi.org/10.1016/j.engfracmech.2023.109079, URL https://www.sciencedirect.com/science/article/pii/S0013794423000371.

[56] Turon A, Camanho PP, Costa J, Renart J. Accurate simulation of delamination growth under mixed-mode loading using cohesive elements: Definition of interlaminar strengths and elastic stiffness. Compos Struct 2010;92(8):1857–64. http://dx.doi.org/10.1016/j.compstruct.2010.01.012.

[57] Bertrand J, Jumel J, Renart J, Kopp JB. Theoretical assessment of ELS test data reduction technique using virtual testing. Int J Fract 2021;229(2):195–213. http://dx.doi.org/10.1007/s10704-021-00549-4.

[58] Cintra GG, Vieira JD, Cardoso DC, Keller T. Mode I and mode II fracture behavior in pultruded glass fiber-polymer – Experimental and numerical investigation. Compos Part B: Eng 2023;266(June):110988. http://dx.doi.org/10.1016/j.compositesb.2023.110988.

[59] Zhao L, Gong Y, Zhang J, Chen Y, Fei B. Simulation of delamination growth in multidirectional laminates under mode I and mixed mode I/II loadings using cohesive elements. Compos Struct 2014;116(1):509–22. http://dx.doi.org/10.1016/j.compstruct.2014.05.042.

[60] Canal LP, Alfano M, Botsis J. A multi-scale based cohesive zone model for the analysis of thickness scaling effect in fiber bridging. Compos Sci Technol 2017;139:90–8. http://dx.doi.org/10.1016/j.compscitech.2016.11.027, URL https://www.sciencedirect.com/science/article/pii/S0266353816317055.

[61] Beetz CP. Strain-induced stiffening of carbon fibres. Fibre Sci Technol 1982;16(3):219–29. http://dx.doi.org/10.1016/0015-0568(82)90035-5, URL https://www.sciencedirect.com/science/article/pii/0015056882900355.

[62] Li X, Monticeli F, Pascoe J-A, Mosleh Y. Interlaminar fracture behaviour of emerging laminated-pultruded CFRP plates for wind turbine blades. Eng Fract Mech 2024;308:110353. http://dx.doi.org/10.1016/j.engfracmech.2024.110353, URL https://www.sciencedirect.com/science/article/pii/S0013794424005162.

[63] Saeedifar M, Zarouchas D. Damage characterization of laminated composites using acoustic emission: A review. Compos Part B: Eng 2020;195:108039. http://dx.doi.org/10.1016/j.compositesb.2020.108039, URL https://www.sciencedirect.com/science/article/pii/S1359836819365096.

[64] Minak G, Zucchelli A. Composite materials research progress. Nova Science Publishers, Inc. 2008, p. 213, Ch. Damage evaluation and residual strength prediction of CFRP laminates by means of acustic emission techniques.

[65] Bakhtiary Davijani A, Hajikhani M, Ahmadi M. Acoustic emission based on sentry function to monitor the initiation of delamination in composite materials. Mater Des 2011;32(5):3059–65. http://dx.doi.org/10.1016/j.matdes.2011.01.010, URL https://www.sciencedirect.com/science/article/pii/S0261306911000136.

[66] de Groot PJ, Wijnen PA, Janssen RB. Real-time frequency determination of acoustic emission for different fracture mechanisms in carbon/epoxy composites. Compos Sci Technol 1995;55(4):405–12. http://dx.doi.org/10.1016/0266-3538(95)00121-2, URL https://www.sciencedirect.com/science/article/pii/0266353895001212.

[67] Biagini D, Pascoe J-A, Alderliesten R. Investigation of compression after impact failure in carbon fiber reinforced polymers using acoustic emission. J Compos Mater 2023;57(10):1819–32. http://dx.doi.org/10.1177/00219983231163853.

[68] Wang C, Vassilopoulos AP, Keller T. Experimental investigation of two-dimensional Mode-II delamination in composite laminates. Compos Part A: Appl Sci Manuf 2023;173(March):107666. http://dx.doi.org/10.1016/j.compositesa.2023.107666.

[69] Huo L, Verstraeten D, Alderliesten RC. Assessment of two quasi-static approaches to mimic repeated impact response and damage behaviour of CFRP laminates. Chin J Aeronaut 2023;36(8):101–14. http://dx.doi.org/10.1016/j.cja.2023.01.015, URL https://www.sciencedirect.com/science/article/pii/S1000936123000201.

[70] Turon A, Camanho PP, Costa J, Dávila CG. A damage model for the simulation of delamination in advanced composites under variable-mode loading. Mech Mater 2006;38(11):1072–89. http://dx.doi.org/10.1016/j.mechmat.2005.10.003.

[71] Ye L. Role of matrix resin in delamination onset and growth in composite laminates. Compos Sci Technol 1988;33(4):257–77. http://dx.doi.org/10.1016/0266-3538(88)90043-7, URL https://www.sciencedirect.com/science/article/pii/0266353888900437.